

University of Louisville

ThinkIR: The University of Louisville's Institutional Repository

Electronic Theses and Dissertations

8-2018

Temperature effects on helium filled soap bubble particle tracking velocimetry.

Michael C. Blum
University of Louisville

Follow this and additional works at: <https://ir.library.louisville.edu/etd>



Part of the [Other Mechanical Engineering Commons](#)

Recommended Citation

Blum, Michael C., "Temperature effects on helium filled soap bubble particle tracking velocimetry." (2018). *Electronic Theses and Dissertations*. Paper 3045.
<https://doi.org/10.18297/etd/3045>

This Master's Thesis is brought to you for free and open access by ThinkIR: The University of Louisville's Institutional Repository. It has been accepted for inclusion in Electronic Theses and Dissertations by an authorized administrator of ThinkIR: The University of Louisville's Institutional Repository. This title appears here courtesy of the author, who has retained all other copyrights. For more information, please contact thinkir@louisville.edu.

TEMPERATURE EFFECTS ON HELIUM FILLED SOAP BUBBLE PARTICLE
TRACKING VELOCIMETRY

By

Michael C. Blum
B.S., University of Kentucky, 2015

A Thesis
Submitted to the Faculty of the
University of Louisville
J.B. Speed School of Engineering
In Partial Fulfillment of the Requirements
for the Degree of
Master of Science
in Mechanical Engineering

Department of Mechanical Engineering
University of Louisville
Louisville, KY

August 2018

TEMPERATURE EFFECTS ON HELIUM FILLED SOAP BUBBLE PARTICLE
TRACKING VELOCIMETRY

By

Michael Christopher Blum
B.S., University of Kentucky, 2015

A Thesis Approved On

July 18, 2018

by the following Thesis Committee:

Dr. Ellen Brehob, Thesis Co-Advisor

Dr. Andrea Kelecy, Thesis Co-Advisor

Dr. Omid Ghasemi Fare, Committee Member

DEDICATION

This thesis is dedicated to my parents, Ruth and Dennis Blum, who have provided me with invaluable educational experiences, and to my fiancé, Stephanie Gammon, who has taught me the strength and courage to continue searching for answers when they are difficult to find.

ACKNOWLEDGMENT

I would like to thank my advisors, Dr. Kelecyc, Dr. Brehob, and James Armstrong, for their unwavering support, knowledge, advice, availability, and encouragement throughout this study. Additionally, I am thankful for management at GE Appliances, including Tim O'Connell and Scott Welham, who have created the opportunities for this project to be sponsored and funded.

ABSTRACT

TEMPERATURE EFFECTS ON HELIUM FILLED SOAP BUBBLE PARTICLE TRACKING VELOCIMETRY

Michael C. Blum

July 18, 2018

Helium Filled Soap Bubble (HFSB) Particle Tracking Velocimetry (PTV) methods are becoming increasingly popular as they provide a low cost, safe option for reliable flow visualization. Several studies have been conducted to understand the accuracy of such systems under normal temperatures and pressures; however, no such studies to date have examined accuracy of HFSB PTV at high temperatures. The goal of this study is to characterize the capability of HFSB PTV methods to visualize air flow through a rectangular duct at elevated temperature.

A heated wind tunnel was designed to heat up to 150 m³/h of 25 °C dry air to 150 °C, and Reynolds numbers ranging from 3500 to 17000 were considered. It was determined that bubble survival at temperatures in excess of 65°C was too low to obtain reliable velocity measurements. In the range of temperatures in which HFSBs survived in adequate numbers, it was demonstrated that Stokes' law was valid and elevated temperatures yielded no significant impact on the ability of HFSBs to trace fluid flow.

TABLE OF CONTENTS

DEDICATION	iii
ACKNOWLEDGMENT	iv
ABSTRACT	v
LIST OF TABLES	viii
LIST OF FIGURES	ix
1 INTRODUCTION AND BACKGROUND.....	1
1.1 General PTV System Overview	2
1.2 Previous Studies of HFSB PTV Accuracy	3
1.3 Bubble Tracer Mechanics.....	4
2 EXPERIMENTAL SETUP AND PROCEDURE	8
2.1 Wind Tunnel Design and Construction	8
2.2 Measurement and Control System Design	11
2.3 Flow Visualization System.....	12
2.4 Verification of Neutrally Buoyant Bubbles.....	15
2.5 Data Analysis and Post Processing.....	15
3 RESULTS.....	18
3.1 Bubble Survival at Temperature	18

3.2	Bubble Accuracy as a Tracer Particle.....	19
3.3	Bubble Survival Rate and Guidelines for Video Length	23
3.4	Bubble Production Repeatability	26
4	CONCLUSIONS	28
	REFERENCES	29
	APPENDICES	32
	Appendix I: Additional Resources.....	33
	Appendix II: Wind Tunnel Design	39
	Appendix III: Flow Visualization System	47
	Appendix IV: Results	56
	Appendix V: Discussion of Heater Induced Buoyancy.....	62
	Appendix VI: Investigation of Boundary Layer Discernment.....	67
	Appendix VII: Effects of Temperature on Bubble Life	71
	CURRICULUM VITA	74

LIST OF TABLES

Table A1: Additional Reading on HFSS PTV.....	33
Table A2: Additional Reading on Wind Tunnel Design.....	37
Table A3: Wind Tunnel BOM.....	43
Table A4: Flow Visualization BOM	47
Table A5: Data Files Exported by MATLAB program.	53

LIST OF FIGURES

Fig. 1 Typical PTV system setup	3
Fig. 2. Stokes number plotted as a function of fluid temperature and Reynolds number	7
Fig. 3. Wind tunnel layout consisting of the heating chamber (A), settling chamber (B), constriction (C), test section (D), and expansion (E).....	9
Fig. 4. Vector Field for 25 °C 3 m/s flow	16
Fig. 5. Streamlines for 25 °C 3 m/s flow	16
Fig. 6. Total bubble count as a function of flow velocity and temperature	19
Fig. 7. Centerline velocity profile for 3 m/s flow	20
Fig. 8. Bubble distribution in the Y direction for 3 m/s flow	22
Fig. 9. Mean Y Velocity Component	23
Fig. A1 Wind tunnel dimensions in mm	39
Fig. A2 Bubble insertion via a cylindrical rake in the heating chamber	40
Fig. A3 Wind tunnel control schematic	42
Fig. A4 Graphical user interface for the LabVIEW system.....	45
Fig. A5 Flow Diagram for LabVIEW control and measurement system	46
Fig. A6 MATLAB image processing program flow chart	52
Fig. A7 Centerline velocity profile for the 1 m/s flow scenario	56
Fig. A8 Centerline velocity profile for the 2 m/s flow scenario	57

Fig. A9 Centerline velocity profile for the 3 m/s flow scenario	57
Fig. A10 Centerline velocity profile for the 4 m/s flow scenario	58
Fig. A11 Centerline velocity profile for the 5 m/s flow scenario	58
Fig. A12 Bubble count in the y direction for the 1 m/s flow scenario.....	59
Fig. A13 Bubble count in the y direction for the 2 m/s flow scenario.....	59
Fig. A14 Bubble count in the y direction for the 3 m/s flow scenario.....	60
Fig. A15 Bubble count in the y direction for the 4 m/s flow scenario.....	60
Fig. A16 Bubble count in the y direction for the 5 m/s flow scenario.....	61
Fig. A17 Heater fin temperature for various power densities [18]	65
Fig. A18 Temperature distribution in the test section for 3 m/s flow	66
Fig. A19 Boundary layer velocity profile for the 1 m/s flow scenario	68
Fig. A20 Boundary layer velocity profile for the 2 m/s flow scenario	68
Fig. A21 Boundary layer velocity profile for the 3 m/s flow scenario	69
Fig. A22 Boundary layer velocity profile for the 4 m/s flow scenario	69
Fig. A23 Boundary layer velocity profile for the 5 m/s flow scenario	70
Fig. A24 Bubble radius as a function of temperature and flow velocity.....	72
Fig. A25 MATLAB bubble detection for 1 m/s 25 °C flow.	73
Fig. A26 MATLAB bubble detection for 5 m/s 25 °C flow.	73

1 INTRODUCTION AND BACKGROUND

Flow visualization methods using tracer particles, such as particle tracking velocimetry (PTV), are commonly used to understand single phase air flow fields of varying complexity. Traditionally, such systems require significant computational resources and high-powered lasers, resulting in high system costs. With advances in computer science, cameras, and light emitting diodes (LEDs), system complexities and cost have been significantly reduced while maintaining similar levels of measurement accuracy. Specifically, a PTV system using helium filled soap bubbles (HFSBs), an LED light sheet, and a MATLAB image processing program, such as that introduced by Tanquero [1], provides advantages by reducing the required computational processing power, eliminating the need for high powered lasers, allowing for simpler system setup, and reducing costs.

Such systems are generally operated at normal temperature and pressure (NTP). Many engineering applications and processes, however, do not occur at NTP. Airflow in a convection oven, dishwasher drying system, HVAC heating system, or a heated greenhouse are just a few examples where engineers and researchers may be interested in visualizing airflow at temperatures greater than NTP. The current paper gives details on the measurement capabilities of a HFSB PTV system when measuring air flows at elevated temperatures.

More specifically a wind tunnel experiment was designed to quantify both the maximum temperature at which bubbles can survive in adequate numbers for valid velocity measurements and the influence of fluid temperature on the tracing fidelity of helium filled soap bubbles for steady, subsonic single phase air flow through a rectangular duct with Reynolds numbers ranging from 3500 to 17000. Three replicates of each test condition were completed to reduce the effects of random error on the experimental results.

1.1 General PTV System Overview

Typical PTV systems consist of four major components: tracer particles (A), a light source (B), a high speed camera (C), and image processing software (D), as illustrated in Fig. 1. The tracer particles are intended to follow all flow characteristics of the fluid of interest and to scatter light such that the tracers may be visible to the camera. The light source provides a thin sheet of light to illuminate tracer particles in a 2D plane of interest. The high speed camera, located perpendicular to the light sheet, captures multiple images of the tracer particles, with each image being separated by a small time period, allowing the tracer particles to move a small distance between each frame. The set of images is processed by the image processing software, in which individual bubbles are tracked and their positions recorded from frame to frame.

Once the physical length that relates to one pixel of the image has been determined, the image processing program calculates the displacement of each tracer particle. Ultimately, with the camera frame rate also known, the velocity of

each tracer particle may be calculated and a velocity field for the flow of interest may be plotted.

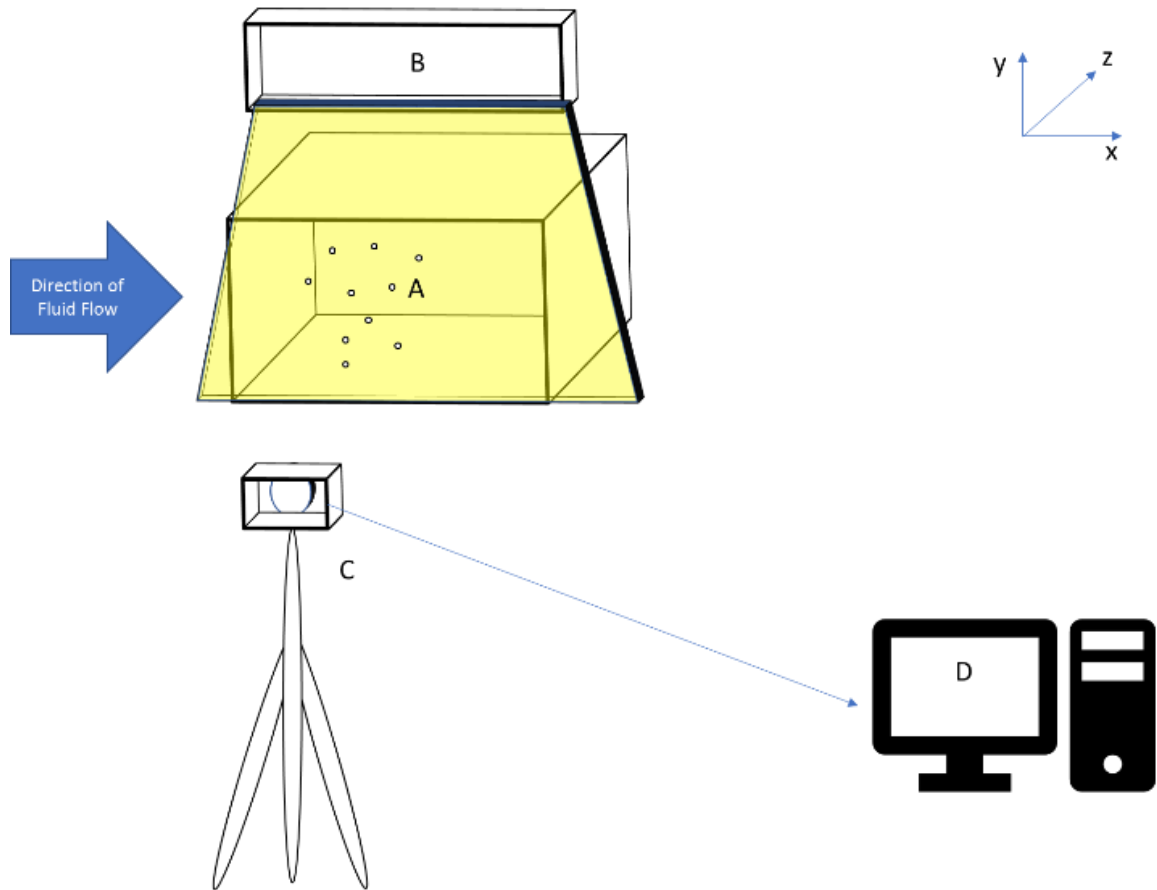


Fig. 1 Typical PTV system setup

1.2 Previous Studies of HFSB PTV Accuracy

HFSBs have been used in a variety of flow visualization studies, ranging from Tanquero's study of air flow through cross flow fans [1] to a CFD validation of mixed convection in a full scale double aisle aircraft cabin performed by Bosbach et al. [2].

However, relatively few studies have focused primarily on the accuracy of HFSB PTV methods. One of the first such studies was completed by Kerho and

Bragg [3], who used millimeter sized HFBSBs to visualize and quantify flow in the stagnation region of a NACA 0012 airfoil at 0° angle of attack. The experimental results from the flow visualization method were compared to flow field streamlines calculated using the Theodorsen method. The HFBSBs were found to deviate slightly from the calculated streamlines, indicating that the bubbles were not neutrally buoyant. To reduce the occurrence of non-neutrally buoyant bubbles, a vortex filter was included in the bubble generator that eliminated bubbles that were denser than air. The authors state in conclusion that the amount of error in HFBSB PTV is highly dependent on the bubble's density ratio and the pressure gradient in the flow, and as such, HFBSB PTV should only be used for qualitative measurements.

Similar to Kerho and Bragg, Scarano et al. [4] measured bubble velocity in the stagnation region of a cylinder to better understand accuracies of HFBSB PTV systems. In contrast to Kerho and Bragg though, Scarano et al. used smaller bubbles with no vortex filter. In comparing the experimental results to flow velocities measured with a particle image velocimetry (PIV) system, the authors state that the characteristic response time of the bubble tracers is approximately 10 μs and conclude that HFBSB PTV may accurately be used for quantitative measurements.

1.3 Bubble Tracer Mechanics

PTV systems calculate the velocity of the tracer particles, not the actual fluid velocity. Therefore, for a PTV system to provide an accurate measurement of fluid

flow, the tracer particle must follow closely the surrounding fluid with little relative motion. To define the motion of a tracer particle, Maxey and Riley [5] defined an equation of motion for a single rigid sphere in non-uniform flow shown in Eq. (1).

$$m_p \frac{d^2 x_p}{dt^2} = \text{Drag} + \text{Bouyancy} + \text{Pressure} + \text{Apparent Mass Force} + \text{Basset Force} \quad (1)$$

Kerho and Bragg [3] used a computational model of Eq. (1) to understand the ability of helium bubble tracer particles of different diameters and densities to accurately trace flow. They determined that for “neutrally” buoyant bubbles, that is bubbles with the same density as air, the pressure force equals the inertial force while the drag, Basset, and buoyant forces are negligible, indicating that such bubbles will follow the fluid path lines ideally.

The assumption of neutrally buoyant bubbles is rarely realized in practical applications, however, as slight variations in gas or soap film solution mass can result in varying bubble densities. Fu et al. [6] indicates that for low Reynolds number flows, Stokes Drag Law, and more specifically Stokes number, is applicable to evaluate the ability of non-neutrally buoyant bubbles to track flow.

Stokes number represents the ratio of the particle response time to the fluid response time as shown in Eq. (2),

$$St = \frac{2 \rho_p}{9 \rho_f} \left(\frac{a}{D_h} \right)^2 Re \quad (2)$$

where ρ_p is the net bubble density, ρ_f is the fluid density, a is the bubble radius, D_h is the hydraulic diameter of the rectangular test section, and Re is the Reynolds number of the flow, defined in Eq. (3). Bubbles will follow the flow field closely if $St < 1$, and particle tracing errors may be less than one percent if $St < 0.1$ [7].

$$Re = \frac{u_{\infty} D_h}{\nu} \quad (3)$$

Using the bubble to fluid density ratio of 0.8 for the 25 °C flow case as reported by Kerho and Bragg [3] as reference, the ratio of bubble density to fluid density can be approximated across the range of temperatures tested as shown in Eq. (4), where $\rho_{f@T_1}$ is the density of the air at the temperature of interest, and $\rho_{f@T=25^{\circ}C}$ is the density of air at 25 °C.

$$\frac{\rho_p}{\rho_f} \approx 0.8 * \frac{\rho_{f@T_1}}{\rho_{f@T=25^{\circ}C}} \quad (4)$$

Utilizing the density ratio defined in Eq. (4) and an average bubble diameter of 1.88 mm found in this study, a conservative calculation of Stokes number was plotted in Fig. 2 for a range of temperatures and Reynolds numbers, assuming a constant bubble density and no heat transfer to the bubble. For all temperatures considered, the calculated Stokes number is below 1.0, suggesting that at elevated temperatures, HFSB should accurately follow the fluid flow if the bubbles can survive at elevated temperatures.

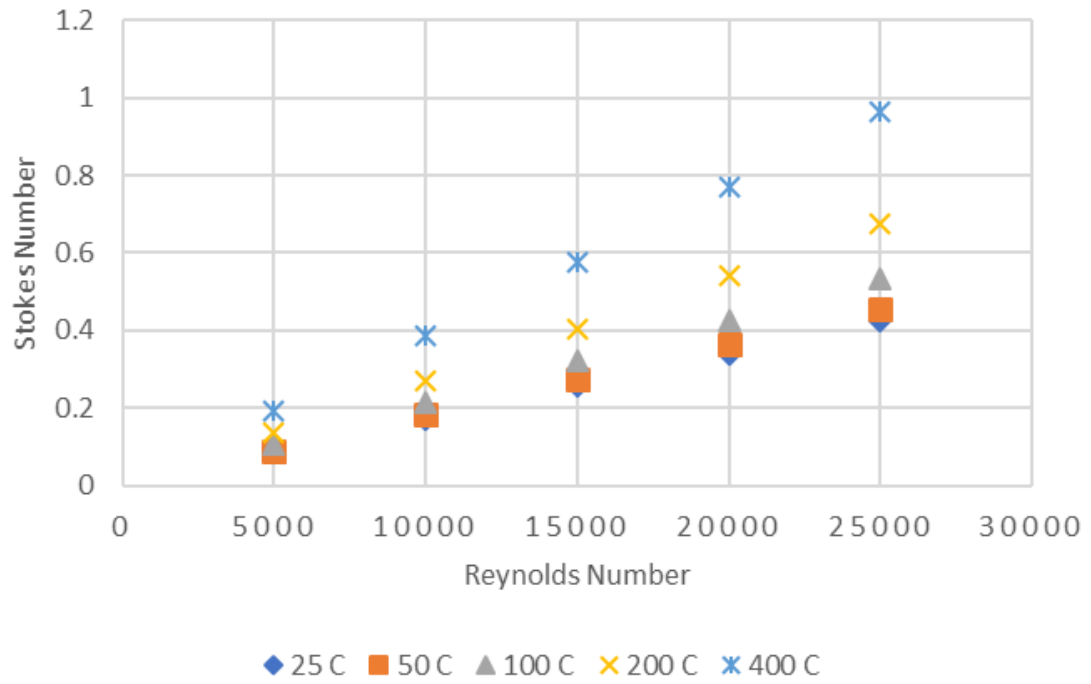


Fig. 2. Stokes number plotted as a function of fluid temperature and Reynolds number

2 EXPERIMENTAL SETUP AND PROCEDURE

A wind tunnel experiment was designed to study the influence of fluid temperature on HFSB tracer fidelity. Beginning at 25°C, steady flow through a rectangular duct was visualized for average velocities ranging from 1 m/s to 5 m/s. Three replicates of each flow scenario were completed one after the other. This process was repeated in 20°C increments until bubbles ceased to survive the increased temperatures in adequate numbers to achieve valid velocity measurements.

2.1 Wind Tunnel Design and Construction

An open loop wind tunnel consisting of a heating section (A), settling chamber (B), constriction (C), test chamber (D), and exit expansion (E) was designed as shown in Fig. 3.

Airflow was pushed through the wind tunnel with an airflow test chamber plenum (not shown) built by Airflow Measurement Systems in accordance with AMCA 210-99. The plenum utilized a variable frequency driven fan capable of providing airflow in excess of 680 m³/hr with no restriction [8]. The open loop wind tunnel design allowed the airflow test chamber to be connected to the inlet of the heating section without concern of plenum components overheating or accumulating soap film solution.

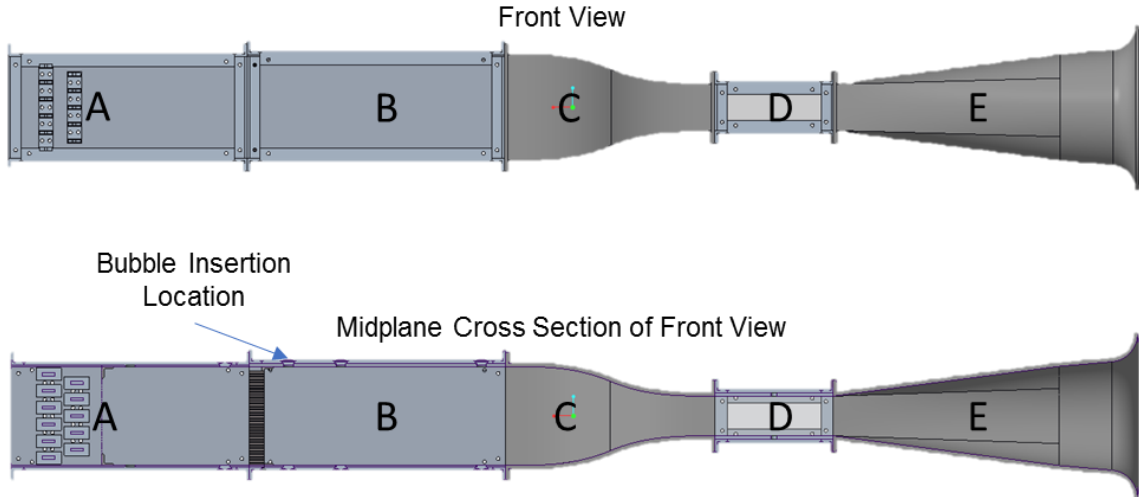


Fig. 3. Wind tunnel layout consisting of the heating chamber (A), settling chamber (B), constriction (C), test section (D), and expansion (E).

The heating chamber, A, was constructed with aluminum walls and was designed with the capability to heat approximately 150 m³/h of 25 °C dry air to 150 °C. Eleven 500-watt Watlow FSP141WMF finned strip heaters were staggered in two rows at the inlet of the heating section to provide 5.5 kW of power to the system. A turbulence generating coarse mesh with a wire diameter of 2.67 mm and a square aperture with side lengths of 10.03 mm was placed immediately downstream of the heaters. The Reynolds number calculated with the mesh wire diameter as the characteristic length remained above 40 for the range of flow velocities tested, indicating the mesh will produce vortices and increase flow turbulence, assisting in flow mixing [9]. A settling length of 20 mesh lengths, or 254 mm, followed the turbulence generating coarse mesh to allow the turbulence to decay before entering the settling chamber [10].

An aluminum wall settling chamber, B, designed to further reduce turbulence was connected to the outlet of the heating chamber using a bolted flanged

connection. An aluminum honeycomb 25.4 mm thick with hexagonal cells 3.175 mm wide was placed at the entrance of the settling chamber. By utilizing a honeycomb with a length to width ratio between seven and ten, incoming flow swirl and lateral flow turbulence was reduced [11], and the hexagonal cell shape allowed bubbles to pass while reducing the pressure drop across the honeycomb [12]. Two additional screens with mesh apertures of 3.35 mm and 2.46 mm respectively were placed immediately downstream of the honeycomb to further reduce turbulence [9]. However, these additional screens popped a significant number of bubbles, and as such the screens were removed during testing. The settling chamber included a settling length of approximately 120 mesh lengths to allow for additional decay of any flow turbulence.

To increase the flow velocity through the test section while further reducing flow turbulence and variations, a contraction, C, was bolted to the outlet of the settling chamber. The shape of the contraction was designed using matched polynomials and an area contraction ratio of 6.25. Contraction ratios greater than four may be sufficient to reduce flow variations to less than two percent [13]. The contraction was 3D printed using a fused deposition modeling (FDM) method with Stratasys's Ultem material, which combines high strength and high heat resistant properties.

The test section, D, measuring 120 mm in width, 80 mm in height, and 240 mm in length was bolted to the outlet of the contraction. The length to width ratio of 1.5 was chosen to reduce the effect of wall interactions on the midplane of the test section [12]. The walls of the test section were composed of transparent glass

to allow visual access of the camera to the flow field and for the light source to illuminate a plane in the flow field normal to the camera. Seven J-type thermocouples were spaced at 12 mm increments in the vertical direction at the outlet of the test section to measure the vertical temperature variation across the test section.

A diffuser, E, was bolted to the exit of the test section to reduce flow turbulence and pressure variations as the flow exited the wind tunnel.

2.2 Measurement and Control System Design

A LabVIEW based data acquisition and control system was developed to control the output power of the Watlow finned heaters and to record system parameters, such as the ambient air temperature, air temperature at the bubble insertion location, air temperature distribution within the test section, and the average air speed at the midpoint of the test section.

The base of the system consisted of a National Instruments cDAQ-9174 chassis, which allowed for up to four different LabVIEW modules to be connected to a computer. An NI 9213 thermocouple module was connected to the chassis to allow for the temperature measurements using J-type thermocouples. The average air speed was measured using the Kanomax 6162 High Temperature anemometer with the Middle Temperature probe 0203, a hot wire anemometer system capable of measuring air speeds in temperatures up to 200 °C. The anemometer system outputs a 0-1 VDC signal, which was read in the LabVIEW program with an NI 9219 analog input module.

The air speed through the test section was controlled manually by adjusting the plenum blower speed using a variable frequency drive (VFD) until the average test section air speed as measured by the Kanomax hot wire anemometer was within 0.05 m/s of the target test air speed.

To maintain a constant air temperature through the test section, a PID control was implemented in LabVIEW to control supplied heater power. The control used as feedback the maximum temperature of the seven thermocouples measuring the temperature in the test section. The PID produced a 4-20 mA output using an NI 9265 analog output module. This variable current signal served as an input to a Watlow DC10-24F0-0000 solid state power control, which generated a pulse width modulation (PWM) signal ranging from 0-100 percent duty cycle based on the current input received from the PID control.

2.3 Flow Visualization System

A PTV system, as illustrated in Fig. 1, using HFSSBs as tracer particles was used as the flow visualization technique in this study. The bubbles were produced by Sage Action Inc.'s SAE Model 5 Helium Bubble Generator, which consisted of a head in which the bubbles were produced and a console which supplied the bubble components to the head.

The head was designed as three concentric tubes. The inner tube carried the helium gas, which filled the bubbles. The middle tube contained the bubble solution, which entrapped the helium gas and formed the physical boundary of the bubble. For this study, SAI 1035 bubble fill solution was used. The bubbles were

pushed off the middle nozzle by compressed air, which was carried through the outer tube [14]. The console contained throttling valves for each of the bubble constituents to control their relative flow, such that bubbles ranging from 1 mm to 4 mm could be produced at rates up to 400 bubbles per second per head [15].

The bubble generating system used in this study contained two heads, each of which released bubbles into a vortex filter that screened bubbles based on density. Bubbles with a net density greater than air were prohibited from passing into the wind tunnel, while bubbles with a net density less than or equal to that of air were permitted to pass into the wind tunnel [3].

Upon exiting the vortex filter, bubbles were inserted into the wind tunnel through a rake placed in the middle of the heating section immediately downstream of the turbulence generating screen. The rake was designed as a hollow steel tube 19 mm in diameter with 7 mm holes drilled at 10 mm increments axially. Each end of the tube was fed independently with bubbles from the two heads, producing a plane of bubbles through the center of the wind tunnel, with a diagram shown in Appendix II: Wind Tunnel Design.

To illuminate the generated bubbles, dark field lighting was used, in which the background of the test section is painted flat black and a light source is placed at an incident angle in the range of 45° to 90° relative to the normal of the plane of interest. Dark field lighting allows for detailed definition of edges of clear objects, such as HFSBs. For this study, an LED light sheet designed by Tanquero [1] with a focal width of approximately 12 mm was placed at an angle of 90° relative to the normal of the plane of interest and in the center of the test section.

High-speed images of the flow field of interest were recorded using a Sony RX100IV digital camera. The 20.1 MP camera allows for high speed videos to be recorded at frame rates of 240 fps, 480 fps, or 960 fps for two or four second durations. For this study, a frame rate of 960 fps was used to reduce bubble shape distortion due to exposure time, and a video duration of four seconds was used to increase the number of bubbles captured.

The high-speed video file was then processed using a Matlab program. Upon opening a video file, the program enabled the user to input the frame rate of the camera as well as the pixel to physical length conversion factor to properly calculate bubble size and flow speed. The images were converted to an 8-bit grayscale value, and a background subtraction algorithm and foreground mask were applied to differentiate object blobs from the background. The centroid of each blob was calculated and tracked frame by frame using a Kalman filter, which predicted the movement of each blob and determined the probability of its next position [16]. The x and y velocity components for each blob were calculated by determining the change in each blob's centroid position between frames and dividing by the camera frame rate as shown in Eq. (5) and Eq. (6).

$$u_x = \frac{x_i - x_{i-1}}{t_{fr}} \quad (5)$$

$$u_y = \frac{y_i - y_{i-1}}{t_{fr}} \quad (6)$$

The x location, y location, radius, number of consecutive detections, x velocity component and y velocity component were recorded for each detection of each blob. To eliminate noise, blobs that were detected in fewer than eight

consecutive frames or blobs that have diameters less than 1 mm or greater than 5 mm were deleted [1].

2.4 Verification of Neutrally Buoyant Bubbles

To create a high number of bubbles small enough to fit through the flow straightening honeycomb, the throttling valves on the bubble generator console were set to 1.067 mm, 0.381 mm and 0.152 mm for the compressed air, bubble solution, and helium gas respectively. These settings produced bubbles with an average diameter of 1.8 mm at a rate in excess of 200 bubbles per second that survived past the honeycomb in the settling chamber of the wind tunnel at 25 °C.

The Stokes number, given in Eq. (2), was then calculated for such a bubble diameter across the range Reynolds numbers tested, assuming a ratio of bubble density to air density of 0.8 at 25 °C as previously noted. For all flow velocities at 25 °C, the calculated Stokes number was less than 0.55, suggesting that the bubble generator parameters used for this study produced nearly neutrally buoyant bubbles at NTP.

2.5 Data Analysis and Post Processing

After analyzing each blob, the MATLAB program divided the first frame from the video file into a grid, with each interrogation window covering approximately a 5mm x 5mm square area. Within each interrogation window, an average x velocity and an average y velocity was calculated by averaging the velocities of each blob detection that passed through the interrogation window throughout the duration of the video. At low velocities, bubbles may have been detected multiple times within

the same interrogation window, and each detection was included in the interrogation window average. The resulting average grid velocities were used to plot the velocity vector field and the streamlines for the flow in the 2D plane of interest, as shown in Fig. 4 and Fig. 5. for the 25 °C 3 m/s flow case.

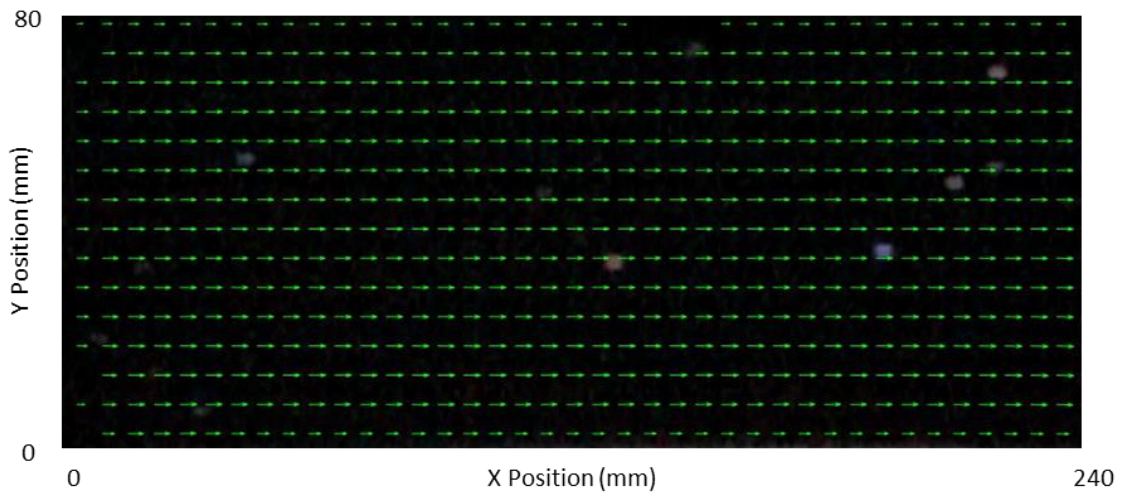


Fig. 4. Vector Field for 25 °C 3 m/s flow

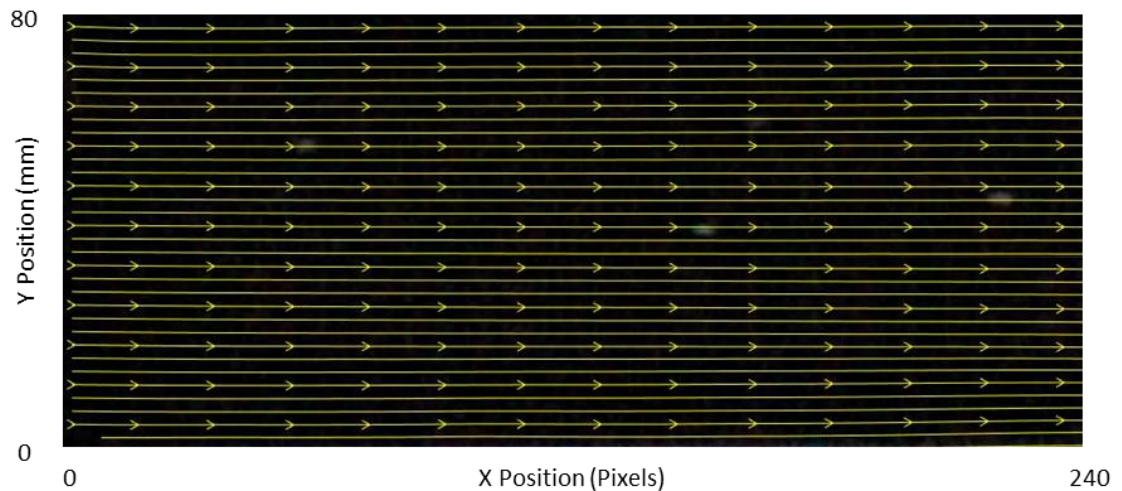


Fig. 5. Streamlines for 25 °C 3 m/s flow

The length of the arrows in the vector plot represents the velocity magnitude. The straightness of the velocity vectors and streamlines in the x-direction indicate

that the bubbles were nearly neutrally buoyant and were accurately following the flow through the rectangular duct.

Additionally, the average centerline velocity profile was plotted and will be further discussed in section 3.2. To better understand the effects of buoyant forces on the HF SBs, the total number of bubbles detected in each row of the grid matrix was counted, providing a plot of the vertical bubble distribution in the test section. Lastly, the total number of detected bubbles were calculated, and the average y velocity component for the entire test section was determined.

3 RESULTS

To quantify the temperature effects on bubble survival rate and response accuracy, the total bubble count, the centerline velocity profile, the bubble distribution in the y direction, and the mean y velocity components were analyzed for each test case.

3.1 Bubble Survival at Temperature

The absolute number of bubbles detected was plotted as a function of flow velocity for each temperature tested as shown in Fig. 6. At a 45 °C maximum test chamber temperature (41 °C average test chamber temperature), approximately half the number of bubbles survived to the test section when compared to the 25 °C flow conditions. At a 65 °C maximum test chamber temperature (56 °C average test chamber temperature), the number of bubbles that survived to the test section of the wind tunnel had dropped to fewer than 60 bubbles, which is less than ten percent of the number of bubbles that survived to the test section in the 25 °C flow conditions. The low survival rate of bubbles indicates that the maximum temperature at which an adequate number of bubbles can survive to provide valid velocity measurements is approximately 65 °C. At this temperature, video lengths must be greatly extended to ensure enough bubbles pass through the test section to accurately measure the average velocity of a steady flow field.

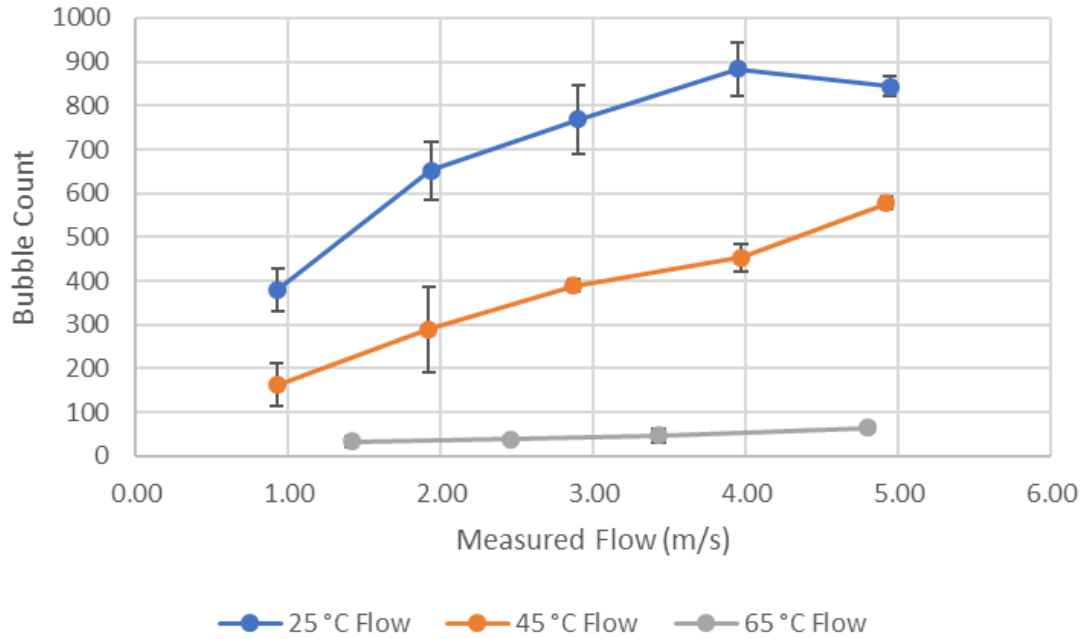


Fig. 6. Total bubble count as a function of flow velocity and temperature

The average bubble diameter was also recorded as a function of temperature and velocity. The bubble size remained nearly constant between the 25 °C, 45 °C, and 65 °C flows for the same bubble generator setting and gas pressures, indicating that the bubbles were not contracting as a function of surrounding fluid temperature. The lack of bubble contraction suggests that evaporation of the bubble film solution rather than excessive stresses imposed on the bubble film solution by an expanding gas is likely the cause for reduced bubble survival rate. Additional discussion of this topic is included in Appendix VII: Effects of Temperature on Bubble Life.

3.2 Bubble Accuracy as a Tracer Particle

To understand the effects of temperature on bubble tracing fidelity, both the centerline velocity profile as well as the mean y velocity component were

compared to the baseline 25 °C test. The 3 m/s centerline velocity plot in Fig. 7 shows nearly identical velocity profiles for the 25 °C and 45 °C flows. The 65 °C flow maximum velocity was similar to that of the other flows, but the overall velocity profile appeared sparse as too few bubbles were recorded to obtain accurate velocity profiles. Further discussion on bubble survival rate is included in section 3.3.

Sparse numbers of bubbles near the walls of the test section across all flow temperatures also resulted in the inability of this method to accurately discern the flow boundary layer. Details on the investigation of the boundary layer may be found in Appendix VI: Investigation of Boundary Layer Discernment.

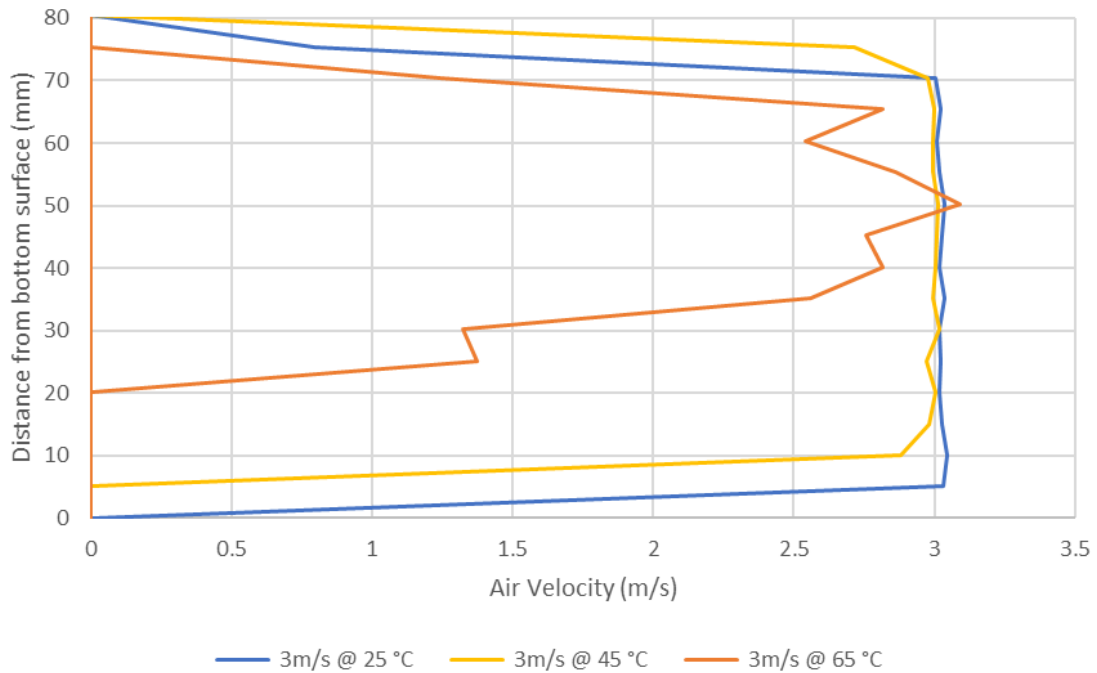


Fig. 7. Centerline velocity profile for 3 m/s flow

A shift of the velocity profile in the positive y direction where y is defined positive up is also apparent in Fig. 7. This shift is caused by the buoyant effects of

cool air moving over the finned strip heaters, causing the flow to stratify over the length of the wind tunnel. This phenomenon can be quantified by calculating the ratio of the Grashoff number to Reynolds number squared, shown in Eq. (7), where Gr is the Grashoff number, Re is the Reynolds number, g is the gravitational constant, β is volumetric thermal expansion coefficient, T_s is the surface temperature, T_∞ is the free stream temperature, D_{hfin} is the hydraulic diameter of the fins defined in Eq. (8) where S is the gap between fins, and u_∞ is the freestream flow velocity.

$$\frac{Gr}{Re^2} = \frac{g\beta(T_s - T_\infty)D_{hfin}}{u_\infty^2} \quad (7)$$

$$D_{hfin} = \frac{S}{2} \quad (8)$$

Assuming a maximum heater output of 500 watts, the heater fin temperature was calculated using the Bar-Cohen and Rosenhow Nusselt correlation, and the ratio of the Grashoff number to Reynolds number squared was determined to be 0.558 for the lowest tested velocities in this study. Ratios near 1 indicate that free convection, or buoyant effects, and forced convection are both significant [17] and show that the shift in the flow velocity was likely due to natural convection of the flow over the heaters rather than non-neutrally buoyant bubbles. Additional details on this calculation are included in Appendix V: Discussion of Heater Induced Buoyancy.

The buoyant driven natural convection over the strip heaters that resulted in flow stratification in the test section can also be seen in the plot of the bubble distribution in the y direction, as shown in Fig. 8. The shift in the positive y direction

due to buoyant effects can be seen as the bubble count profiles shift in the positive y direction with increasing temperature.

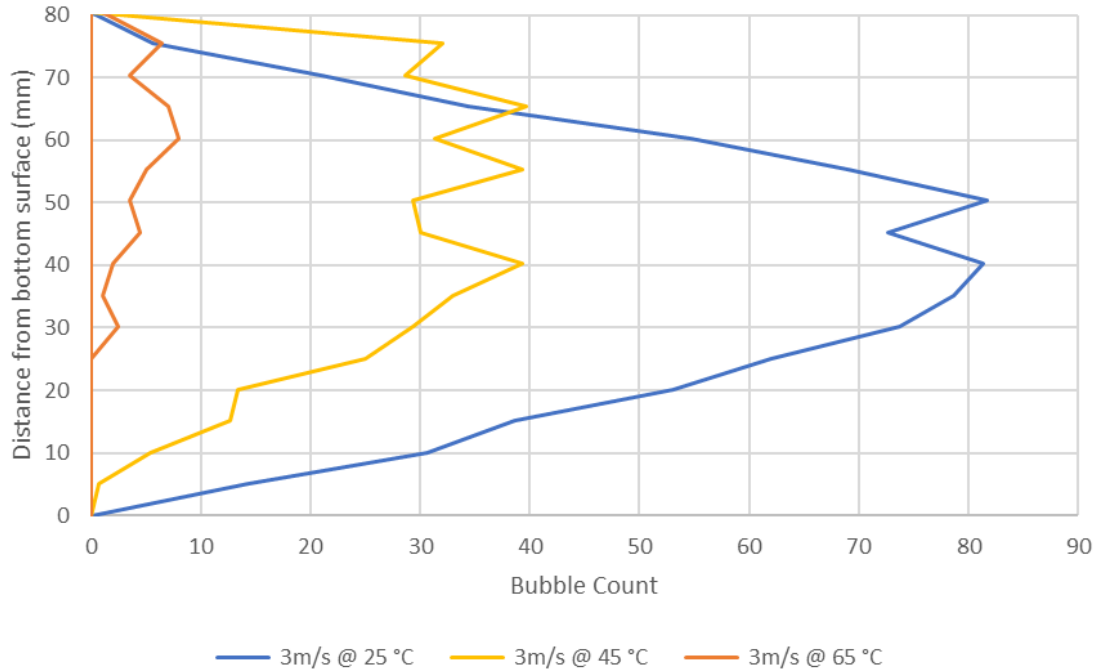


Fig. 8. Bubble distribution in the Y direction for 3 m/s flow

While results are only shown for the 3 m/s flow case, results were similar across all flow scenarios tested, and complete results may be found in Appendix IV: Results.

To ensure buoyant effects did not impart an unexpected motion in the HFBSs in the y direction, the mean y velocity component was plotted as a function of measured mean flow velocity across the range of temperatures tested, as shown in Fig. 9. Errors bars are included to show the 95 percent confidence interval for each test case. The overlapping of the confidence intervals shows there is no statistically significant difference in the mean y velocity component across the range of flow temperatures tested, further confirming the Stokes number

calculation indicating that increased temperatures do not alter the ability of HFBSBs to accurately trace air flow.

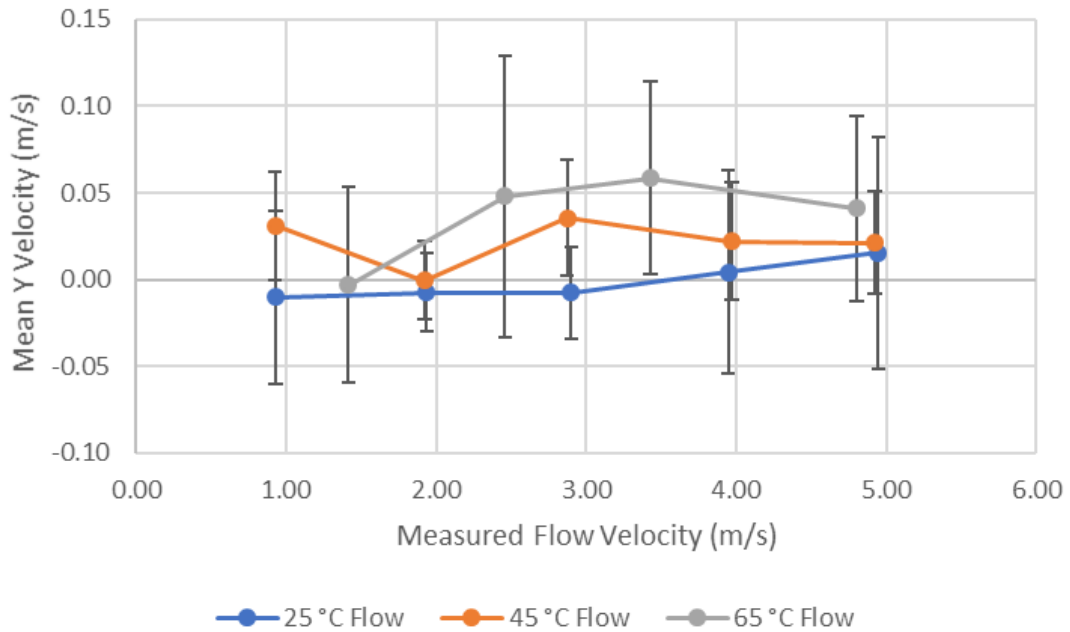


Fig. 9. Mean Y Velocity Component

3.3 Bubble Survival Rate and Guidelines for Video Length

The ability of the HFBSB PTV system to accurately measure the velocity of a steady flow field is highly dependent on the number of bubbles captured by the high speed camera in the region of interest. As seen in Fig. 7, the centerline velocity profile is well defined for the 25 °C and 45 °C flow scenarios, in which the total bubble count exceeded 300 bubbles. Conversely, the centerline velocity profile for the 65°C flow scenario is not well defined due to the sparse number of bubbles that survived at that temperature, merely 60 bubbles.

For a fixed set of bubble generator parameters and fixed flow velocity, the only way to increase the captured bubble count is to either increase the length of

time of the video or to decrease the distance in which the bubbles must pass before entering the region of interest. To better define either the required video time or the allowable length for bubbles to travel before entering the test section, a method for determining the bubble survival rate was developed.

At each temperature tested, the bubble survival rate was calculated by first determining the distance the bubbles traveled before entering the test section. For this study, the bubbles traveled 1.31 m before entering the test section. The distance traveled, $L_{travelled}$, was divided by the measured freestream flow velocity to find the required bubble survival time, $t_{survival}$, as shown in Eq. (9).

$$t_{survival} = \frac{L_{travelled}}{u_{\infty}} \quad (9)$$

The number of bubbles generated per second that existed at the required survival time was calculated by dividing the total number of bubbles recorded by the video time length, which for this study was four seconds. The number of bubbles produced per second that survived at least the minimum required survival time were then plotted as a function of the required survival time, as shown in Fig. 10. When compared to the 25 °C flow cases, approximately half of the number of bubbles survived at 45 °C, and fewer than ten percent survived at 65 °C.

A regression equation that calculated the number of bubbles produced per second as a function required survival time was generated for each temperature tested and are given as Eq. (10) – Eq. (12).

$$BPS_{25C} = -77.55 \ln(t_{survival}) + 123.28 \quad (10)$$

$$BPS_{45C} = -60.82 \ln(t_{survival}) + 51.954 \quad (11)$$

$$BPS_{65C} = -7.939 \ln(t_{survival}) + 4.1968 \quad (12)$$

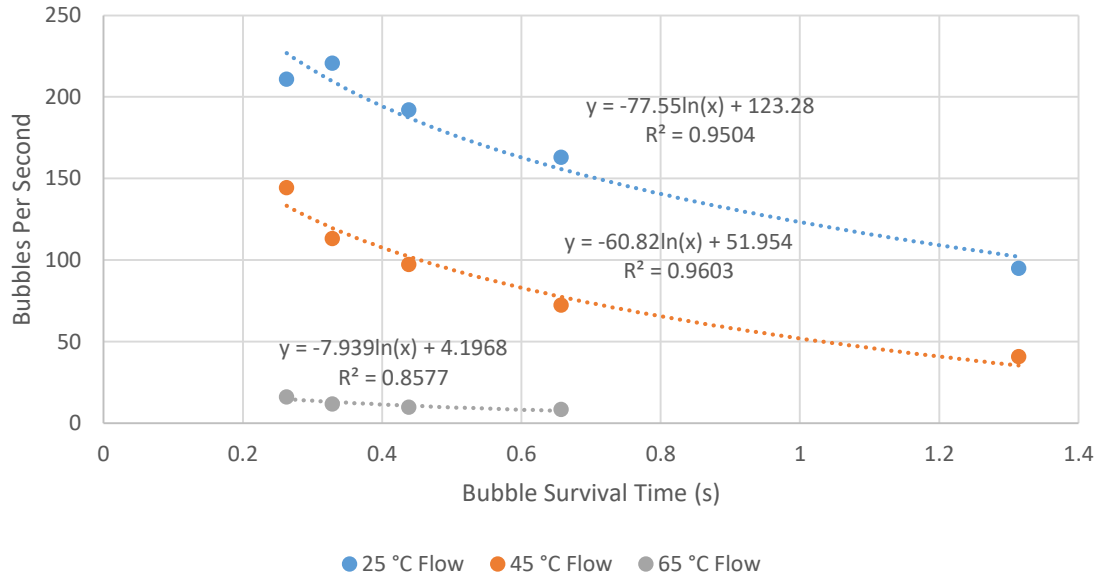


Fig. 10. Bubble Survival Rate

To determine the bubble resolution required to measure accurate bubble velocities, the centerline profiles for each test case were considered. Except for the 65 °C flow cases, all centerline velocity profiles were well defined with the exception of the 45 °C 1 m/s flow, in which only 163 bubbles were detected on average. Therefore, for clearly defined flow profiles, a minimum of 300 detected bubbles should be targeted as indicated in Fig. 6.

The minimum required video length may then be calculated by first determining the required bubble survival time per Eq. (9). The number of bubbles produced per second that will survive the required time may be determined from either Eq. (10) - Eq.(12) depending on the fluid temperature. Lastly, the video length may be calculated by Eq. (13), where t_{video} is the required video length, and

$Bubbles_{TargetNumber}$ is the targeted 300 total number of bubbles to pass through the test section.

$$t_{video} = \frac{Bubbles_{TargetNumber}}{BPS} \quad (13)$$

For the 65°C 3 m/s flow case, the required video length calculated using Eq. (13) is 27.8 s, nearly seven times the length of video used for this study. Eq. (10) - Eq. (12) are only valid for the set of bubble constituent parameters used in this study, and they should be redefined for different sets of bubble parameters. Additionally, due to the required video length, the detailed method is only valid for steady flows.

3.4 Bubble Production Repeatability

After the first set of tests, the 25 °C 3 m/s flow scenario was repeated in an additional set of three consecutive runs to understand the repeatability of bubble production over time. The initial set of tests yielded an average of 768 bubbles with a MATLAB calculated diameter of 2.9 mm, while the repeated set of tests yielded an average of 246.7 bubbles with a MATLAB calculated diameter of 1.8 mm. This significant difference in bubble count and bubble diameter, 68% and 35% respectively, initially indicates that the bubble production technique yields poor repeatability. However, between the first set of tests and the repeated set of tests, the helium gas pressure had been reduced by an order of magnitude from 10.34 MPa to 0.69 MPa. The pressure loss was due to a slow gas leak in the helium tank over a period of months. During normal testing conditions, such as the first set of tests, the pressure loss in the helium tank was negligible. It should

be noted that due to the frame rate of the camera, the MATLAB calculated bubble diameter is overestimated at elevated flow velocities, explaining the difference between the reported 1.8 mm average bubble diameter for the first set of tests reported in section 2.4 and the 2.8 mm calculated bubble diameter for the first set of tests used for this repeatability study. Additional details on the effects of bubble velocity on the calculated bubble diameter may be found in Appendix VII: Effects of Temperature on Bubble Life.

To account for the pressure difference between the first and second set of tests, the 25 °C 3 m/s test was repeated a third time in another set of three consecutive runs, while maintaining the helium gas pressure at approximately 0.69 MPa, similar to the second set of tests. The third set of tests yielded an average bubble count of 247 bubbles with a MATLAB calculated bubble diameter of 1.6 mm. The bubble count and bubble diameter were only 0.7 % and 10.2% different respectively between the second and third set of tests. This suggests that if the bubble constituent material levels are kept nearly constant, bubble production is repeatable. However, if large variations in bubble fill solution or helium gas pressure occur, the bubble quality will vary. Additional studies need to be conducted to quantify the effects of helium pressure on bubble parameters.

4 CONCLUSIONS

It was determined that HF SBs do not survive in 65 °C flow at a high enough rate to provide valid velocity measurements, unless the test is run for an extended period of time. Up to this temperature though, Stoke's theory was confirmed, and it was determined that the ability of HF SBs to accurately follow fluid flow was not significantly affected by fluid temperature. Additionally, a method for calculating the required video length to ensure high bubble count was described, providing a means to obtain accurate and detailed velocity profiles even with low bubble survival rates. Lastly, it was determined that HF SBs could be produced with high levels of repeatability given the levels of bubble constituents are held constant.

This study focused solely on flow through a rectangular duct with no additional pressure gradients. The work of Kerho and Bragg suggests, however, that additional pressure gradients can affect the ability of HF SBs to accurately follow flow. Future studies on the effects of temperature on tracing fidelity of HF SBs should include tests with added pressure gradients and flow disturbances. Additionally, further research is needed to understand if bubble survival rates may be increased by any of the following means: adjusting parameters of the bubble generating console, studying the evaporation rates of different bubble film solutions, and preheating bubble constituents prior to bubble generation.

REFERENCES

- [1] Y. Tanquero, "A Performance and Visualization Study On Inlet Geometries of A Cross-Flow Fan," Louisville, KY, 2017.
- [2] J. Bosbach, M. Kuhn and C. Wagner, "Large Scale Particle Image Velocimetry with Helium Filled Soap Bubbles," *Exp Fluids*, vol. 46, pp. 539-547, 2009.
- [3] M. F. Kerho and M. B. Bragg, "Neutrally Bouyant Bubbles Used As Flow Tracers in Air," *Experiments in Fluids*, pp. 393-400, 1994.
- [4] F. Scarano, S. Ghaemi, G. Caridi, J. Bosbach, U. Dierksheide and A. Sciacchitano, "On the Use of Helium Filled Soap Bubbles for Large Scale Tomographic PIV in Wind Tunnel Experiments," *Exp Fluids*, vol. 56, no. 42, 2015.
- [5] M. R. Maxey and J. J. Riley, "Equation of Motion for a Small Rigid Sphere in a Nonuniform Flow," *Physics of Fluids*, pp. 883-889, 1983.

- [6] S. Fu, P. H. Biwole and C. Mathis, "Particle Tracking Velocimetry for Indoor Airflow Field: a Review," *Building and Environment*, vol. 87, pp. 34-44, 2015.
- [7] C. Tropea, A. Yarin and J. Foss, Springer Handbook of Experimental Fluid Mechanics, Berlin: Springer-Verlag, 2007.
- [8] Airflow Measurement Systems, "Instruction Manual For AMCA 210-99 Airflow Test Chamber," Chula Vista, California, 2011.
- [9] M. Johl, M. Passmore and P. Render, "Design Methodology and Performance of an Indraft Wind Tunnel," *The Aerunautical Journal*, vol. 108, pp. 465-47, 2004.
- [10] J. Groth and A. V. Johansson, "Turbulence Reduction by Screens," *J. Fluid Mech.*, vol. 197, pp. 139-155, 1988.
- [11] L. Cattafesta, C. Bahr and J. Mathew, "Fundamentals of Wind-Tunnel Design," in *Encyclopedia of Aerospace Engineering*, John Wiley & Sons, Ltd., 2010.
- [12] W. H. J. Rae and A. Pope, Low-Speed Wind Tunnel Testing, 2nd ed., New York: John Wiley & Sons, 1984.
- [13] M. Hernandez, A. Lopez, A. Jarzabek, J. Perales, Y. Wu and S. Xiaoxiao, "Design Methodology for a Quick and Low Cost Wind Tunnel," in *Wind*

Tunnel Designs and Their Diverse Engineering Applications, Intech, 2013.

- [14] R. Hale, "Development of An Integrated System For Flow Visualization in Air Using Neutrally-Bouyant Bubbles," National Technical Information Service U.S. Department of Commerce, Springfield, 1971.

- [15] Sage Action, Inc., "Bubble Generator Systems Air Flow Visualization and Measurement," Sage Action, Inc., Apache Junction, 2017.

- [16] The Mathworks, Inc., "Motion-Based Multiple Object Tracking," MathWorks, 2018. [Online]. Available: <https://www.mathworks.com/help/vision/examples/motion-based-multiple-object-tracking.html>. [Accessed 17 April 2018].

- [17] T. Bergman, A. S. Lavine, F. P. Incropera and D. P. Dewitt, *Fundamentals of Heat and Mass Transfer*, 7th ed., Hoboken: John Wiley & Sons, 2011.

- [18] Watlow, "What type of heater do you need?," 07 November 2011. [Online]. [Accessed 09 July 2018].

APPENDICES

Appendix I: Additional Resources.....	33
Appendix II: Wind tunnel Design.....	39
Appendix III: Flow Visualization System	47
Appendix IV: Results	56
Appendix V: Discussion of Heater Induced Buoyancy.....	62
Appendix VI: Investigation of Boundary Layer Discernment.....	67
Appendix VII: Effects of Temperature on Bubble Life	71

Appendix I: Additional Resources

Further information regarding HFSB PTV may be found below in Table A1.

Table A1: Additional Reading on HFSB PTV.

Reference	Summary
<p>Alharbi, Ali, and Volker Sick. "Investigation of Boundary Layers in Internal Combustion Engines Using a Hybrid Algorithm of High Speed Micro-PIV and PTV." <i>Exp Fluids</i>, 2010: 949-959.</p>	<p>Micro particle image velocimetry (μPIV) and particle tracking velocimetry (PTV) are used to study the dynamics of boundary layer flow in an internal combustion engine. Results suggest there is significant variation in flow behavior between strokes, and millimeter sized vortical structures were visualized within the boundary layer.</p>
<p>Bergman, Theodore, Adrienne S. Lavine, Frank P. Incropera, and David P. Dewitt. <i>Fundamentals of Heat and Mass Transfer</i>. 7th. Hoboken: John Wiley & Sons, 2011.</p>	<p>Heat transfer text book provides details on mixed, forced, and natural convective heat transfer, as well as numerous other heat transfer topics.</p>
<p>Bosbach, Johannes, Matthias Kuhn, and Claus Wagner. "Large Scale Particle Image Velocimetry with Helium Filled Soap Bubbles." <i>Exp Fluids</i> 46 (2009): 539-547.</p>	<p>Helium filled soap bubbles are used in conjunction with high powered solid state lasers to conduct PIV measurements in a several square meter area in an aircraft cabin. The authors discuss the benefits of using small bubbles as well as the need to increase video length due to low bubble density.</p>

<p>Cao, Xiaodong, Junjie Liu, Nan Jiang, and Qingyan Chen. "Particle Image Velocimetry Measurement of Indoor Airflow Field: A Review of the Technologies and Applications." <i>Energy and Buildings</i>, 2014: 367-380.</p>	<p>A summary of typical PIV systems used for indoor environments is provided. Additionally, the authors provide details on typical parameters for PIV systems as well as potential accuracy of such systems.</p>
<p>Caridi, Giuseppe, Daniele Ragni, Andrea Sciacchitano, and Fulvio Scarano. "HFSB-Seeding for Large-scale Tomographic PIV in Wind Tunnels." <i>Exp Fluids</i>, 2016.</p>	<p>A novel PIV system is introduced using sub millimeter sized HFSBs to study flow in large-scale environments. The system details the required bubble spatial resolution, methods to achieve high bubble density using a holding tank for generated bubbles, and methods to introduce the bubbles in a wind tunnel via an aerodynamic rake.</p>
<p>Faleiros, David, Marthjun Tuinstra, Andrea Sciacchitano, and Fulvio Scarano. "Helium-Filled Soap Bubble Tracing Fidelity in Wall-Bounded Turbulence." <i>Experiments in Fluids</i>, 2018.</p>	<p>Helium filled soap bubbles are used to measure properties of the turbulent boundary layer on wall bounded flows. The study suggests that HFSBs may be used as accurate tracer particles to quantify mean velocity and turbulence fluctuations up to a distance of two bubble diameters from the wall.</p>
<p>Fu, Sijie, Pascal Henry Biwole, and Christian Mathis. "Particle Tracking Velocimetry for Indoor Airflow Field: a Review." <i>Building and Environment</i> 87 (2015): 34-44.</p>	<p>A general overview of PTV systems is discussed including details on lighting, tracer particles, particle response, camera systems, and tracking algorithms. The authors also include a summary of relevant PTV studies for indoor airflow.</p>
<p>Hale, R.W. <i>Development of An Integrated System For Flow Visualization in Air Using Neutrally-Bouyant Bubbles</i>. Sage Action, Incorporated, Springfield: National Technical Information Service U.S. Department of Commerce, 1971.</p>	<p>This document was written for the Naval Research Office and includes in depth details to the development of the SAI HFSB generator. Additionally, the study highlights component design, system evaluation, and some wind tunnel testing.</p>

<p>Kerho, Michael F., and Michael B. Bragg. "Neutrally Bouyant Bubbles Used As Flow Tracers in Air." <i>Experiments in Fluids</i>, 1994: 393-400.</p>	<p>The stagnation region of air flow past an NACA 0012 airfoil is used to study the accuracy of HFSB in tracing fluid flow. The authors determined that if the bubbles are neutrally buoyant, they will perfectly follow the flow. However, differences in buoyancy will create errors dependent on the bubble density ratio and the local pressure gradient. Based on their system, the authors recommend HFSB PTV be used only for qualitative measurements, not quantitative measurements.</p>
<p>Maxey, Martin R., and James J. Riley. "Equation of Motion for a Small Rigid Sphere in a Nonuniform Flow." <i>Physics of Fluids</i>, 1983: 883-889.</p>	<p>A model is developed for the motion of a small rigid sphere in a non-uniform flow. This model was used by Kerho and Bragg.</p>
<p>Morias, Koen, Giuseppe Caridi, Andrea Sciacchitano, and Fulvio Scarano. "Statistical Characterization of Helium-filled Soap bubbles Tracing Fidelity for PIV." <i>18th International Symposium on the Application of Laser and Imaging Techniques to Fluid Mechanics</i>. Lisbon, 2016.</p>	<p>The statistical accuracy of a HFSB PTV method is determined by comparing the HFSB PTV results to fog droplet PIV results in the stagnation region of flow over a cylinder. The authors complete a statistical analysis of the bubble slip velocity, bubble relaxation time, bubble diameter, and bubble density. The authors conclude that HFSB can provide high accuracy measurements for time-averaged flows, but accuracy may be decreased for instantaneous and fluctuating flows.</p>
<p>Sage Action, Inc. <i>Bubble Generator Systems Air Flow Visualization and Measurement</i>. Apache Junction: Sage Action, Inc., 2017.</p>	<p>A reference manual highlighting the system components of the SAI HFSB generator, operating procedures, and methods to adjust bubble properties.</p>

<p>Scarano, Fulvio, Sina Ghaemi, Giuseppe Caridi, Johannes Bosbach, Uwe Dierksheide, and Andrea Sciacchitano. "On the Use of Helium Filled Soap Bubbles for Large Scale Tomographic PIV in Wind Tunnel Experiments." <i>Exp Fluids</i> 56, no. 42 (2015).</p>	<p>The stagnation region of air flow past a cylinder is used to determine the accuracy of HFSB PTV. The authors conclude that the average characteristic response time of HFSBs is approximately 10 μs, and as such, HFSB PTV provides high accuracy quantitative measurements of time-averaged fluid flows.</p>
<p>Tanquero, Yoel. "A Performance and Visualization Study On Inlet Geometries of A Cross-Flow Fan." Louisville, KY, 2017.</p>	<p>A low cost HFSB PTV system is detailed using the SAI HFSB generator, a MATLAB software program, and an LED light source. The author uses the HFSB PTV system to identify critical design geometries for cross flow fan inlets.</p>
<p>Tavoularis, Stavros. <i>Measurements in Fluid Mechanics</i>. New York: Cambridge University Press, 2005.</p>	<p>Text book in experimental fluids detailing wind tunnel design as well as PTV and PIV techniques.</p>
<p>The Mathworks, Inc. <i>Motion-Based Multiple Object Tracking</i>. MathWorks. 2018. https://www.mathworks.com/help/vision/examples/motion-based-multiple-object-tracking.html (accessed April 17, 2018).</p>	<p>Mathworks documentation providing details on MATLAB's multiple object tracking algorithm and the use of Kalman filters.</p>
<p>Tropea, Cameron, Alexander Yarin, and John Foss. <i>Springer Handbook of Experimental Fluid Mechanics</i>. Berlin: Springer-Verlag, 2007.</p>	<p>Text book in experimental fluids detailing PTV and PIV techniques as well as particle response time.</p>

Further reading on wind tunnel design may be found in Table A2.

Table A2: Additional Reading on Wind Tunnel Design.

Reference	Summary
<p>Airflow Measurement Systems. "Instruction Manual For AMCA 210-99 Airflow Test Chamber." Chula Vista, California, 2011.</p>	<p>Documentation for the Air Flow Measurement System detailing plenum components, nozzle arrangements, and methods to take volumetric flow rate measurements for fan and system curves.</p>
<p>Cattafesta, Louis, Chris Bahr, and Jose Mathew. "Fundamentals of Wind-Tunnel Design." In <i>Encyclopedia of Aerospace Engineering</i>. John Wiley & Sons, Ltd., 2010.</p>	<p>General discussion highlighting wind tunnel design, including drive systems, ducting, flow conditioners, and contractions.</p>
<p>Groth, Johan, and Arne V. Johansson. "Turbulence Reduction by Screens." <i>J. Fluid Mech.</i> 197 (1988): 139-155.</p>	<p>An investigation on the effects of mesh screen parameters and the number of screens to reduce turbulence in wind tunnels.</p>
<p>Hernandez, Miguel, Ana Lopez, Artur Jarzabek, Jose Perales, Yuliang Wu, and Sun Xiaoxiao. "Design Methodology for a Quick and Low Cost Wind Tunnel." In <i>Wind Tunnel Designs and Their Diverse Engineering Applications</i>. Intech, 2013.</p>	<p>An overview of wind tunnel design discussing general requirements of wind tunnel components including the test section, contraction, settling chamber, diffuser, corners, and drive system.</p>
<p>Johl, M., M. Passmore, and P. Render. "Design Methodology and Performance of an Indraft Wind Tunnel." <i>The Aeronautical Journal</i> 108 (2004): 465-47.</p>	<p>Details explaining the design requirements and methodology of the Loughborough University wind tunnel. Quantification of wind tunnel performance is also included.</p>

<p>Rae, Willam H. Jr., and Alan Pope. <i>Low-Speed Wind Tunnel Testing</i>. 2nd. New York: John Wiley & Sons, 1984.</p>	<p>Text book detailing wind tunnel design, instrumentation, measurements, and common testing procedures.</p>
<p>Tavoularis, Stavros. <i>Measurements in Fluid Mechanics</i>. New York: Cambridge University Press, 2005.</p>	<p>Text book in experimental fluids detailing wind tunnel design as well as PTV and PIV techniques.</p>
<p>Tropea, Cameron, Alexander Yarin, and John Foss. <i>Springer Handbook of Experimental Fluid Mechanics</i>. Berlin: Springer-Verlag, 2007.</p>	<p>Text book in experimental fluids detailing PTV and PIV techniques as well as particle response time.</p>

Appendix II: Wind Tunnel Design

The overall dimensions for critical components of the wind tunnel may be found in Fig. A1. CAD files and drawings for individual wind tunnel components are available upon request.

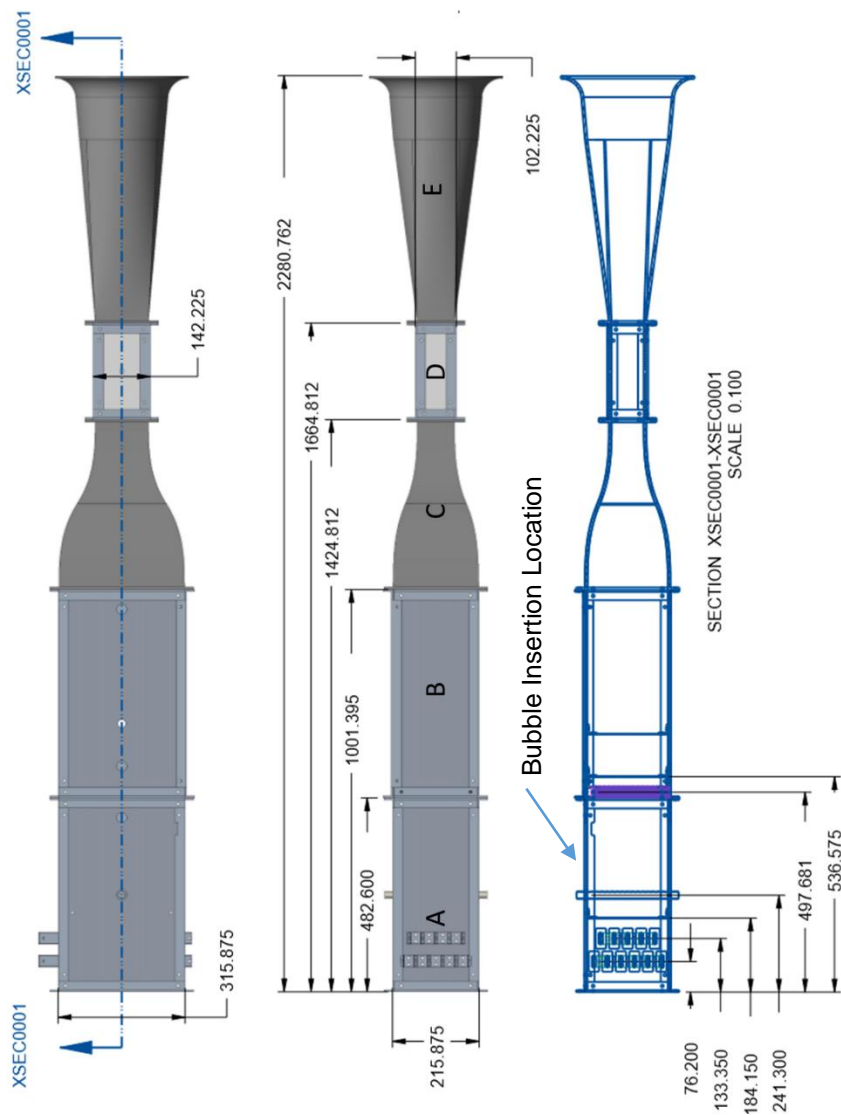


Fig. A1 Wind tunnel dimensions in mm

Section A represents the heating chamber of the wind tunnel. Within the heating chamber are eleven, 500 W finned strip heaters arranged in two rows. Immediately following the heaters, a turbulence generating mesh screen is found to promote flow mixing. The HF SBs are injected into the flow shortly downstream of the turbulence generating grid via a hollow steel tube 19 mm in diameter with 7 mm holes drilled at 10 mm increments axially, as depicted in Fig. A2. Bubbles were fed from the bubble generator into both ends of the cylindrical rake, reducing the pressure variation across the rake outlet holes and producing a more uniform plane of bubbles through the wind tunnel. Details on the remaining components of the wind tunnel may be found in Section 3.1, “Wind tunnel Design and Construction.”

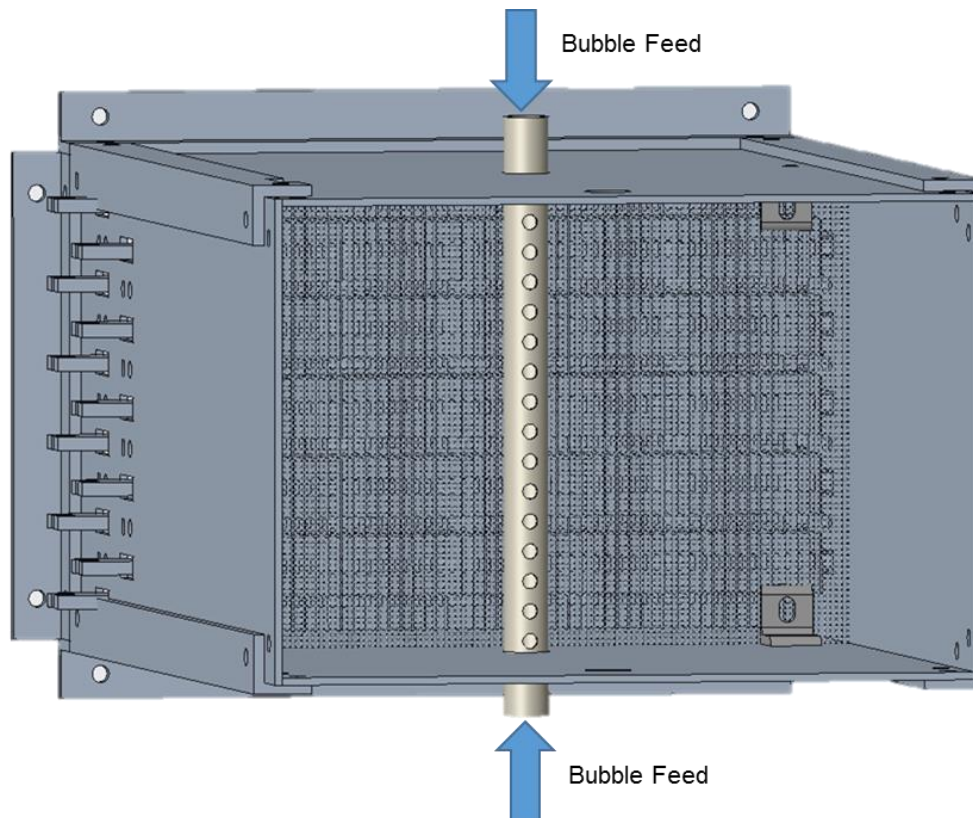


Fig. A2 Bubble insertion via a cylindrical rake in the heating chamber

The wind tunnel heaters, control system, and measurement system were powered with a 240V, 3 pole power supply, as illustrated in the control schematic given in Fig. A3. Upon entering the electronics enclosure, an emergency stop button was wired in series with L1, which then served to power an electromagnetic contactor. L1, L2, and N were then wired to the input of the contactor, such that if the emergency stop is pressed, power will be cut to the contactor, which will in turn create an open circuit between L1, L2, N and the rest of the electronic circuitry.

Upon exiting the contactor, L1 was wired to a 50A circuit breaker before being connected to the solid-state power control, which modulated the 120V L1 signal via a pulse width modulation (PWM) technique. The duty cycle of the PWM signal output from the power control to the heaters was determined from a PID control that will be discussed and a 0-20 milliamp analog signal from the LabVIEW NI 9265 analog output module.

L2 served to power a 24 VDC power supply, which in turn provided power for the remaining measurement and control devices. More specifically, the 24 VDC power supply provided power to the LabVIEW cDAQ 9174 chassis, which served as the primary electronic hub for the LabVIEW control and measurement system used for this study.

Connected to the LabVIEW chassis was an NI 9265 analog output module that provided a milliamp analog signal to control the duty cycle of the solid state power control. The NI 9219 analog input module connected to the chassis allowed for data acquisition of the temperature and velocity from the hot wire anemometer system. Lastly, a thermocouple module, the NI 9213, was connected to the

chassis to allow for temperature readings throughout the wind tunnel. The bill of materials (BOM) for the wind tunnel may be found in Table A3.

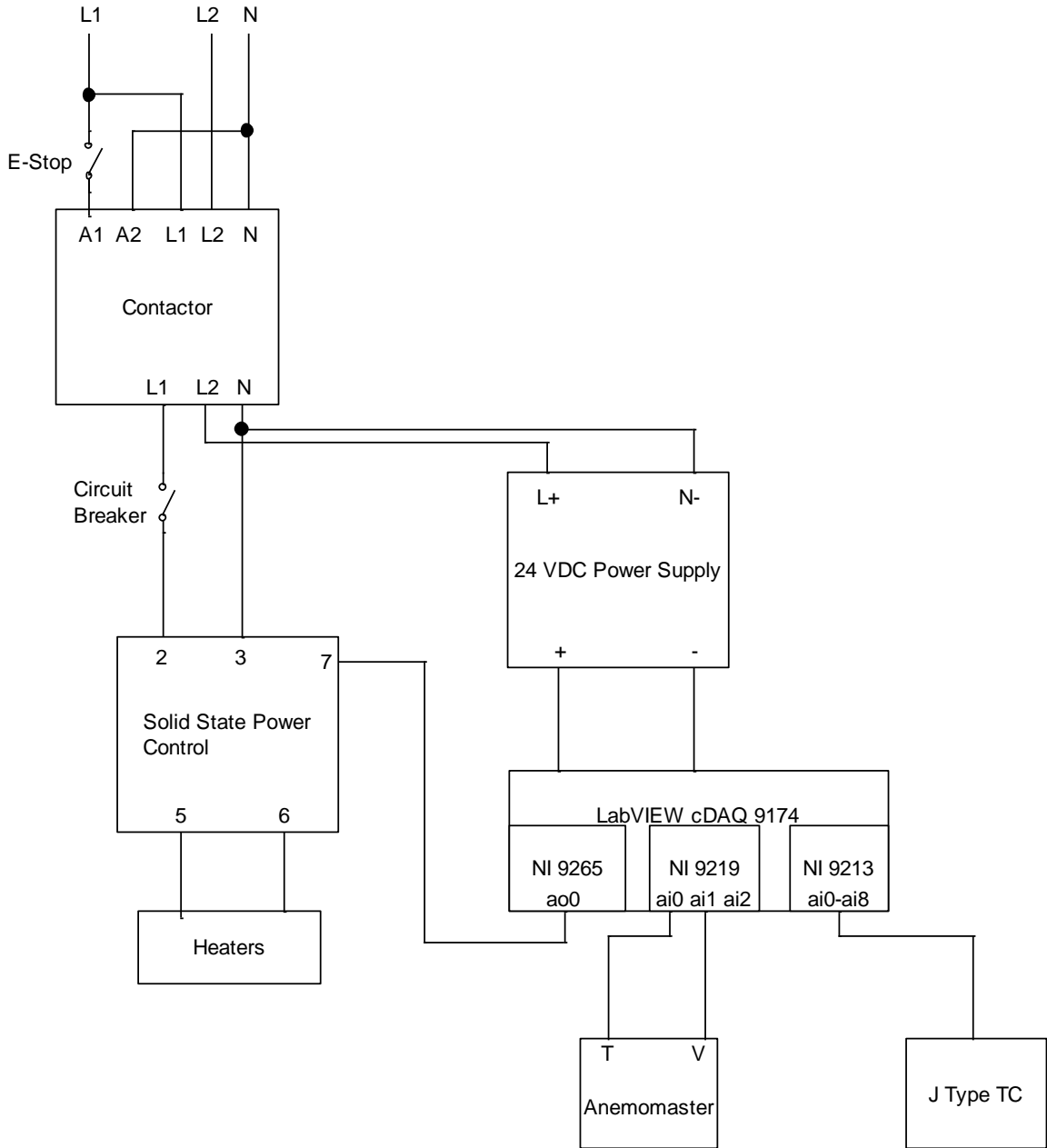


Fig. A3 Wind tunnel control schematic

Table A3: Wind Tunnel BOM

Item	Manufacturer	Part Number	Qty
Heaters	Watlow	FSP141WMF-1	11
Solid State Power Control	Watlow	DC10-24F0-0000	1
Contactator	Allen Bradley	100-C37*00	1
Circuit Breaker	Eaton	FAZ-C50/1	1
E Stop	Eaton	E22B1	1
24VDC Power Supply	Omron	S8VK-G01524	1
Anemometer Control and DAQ	Kanomax	6162	1
Anemometer Probe	Kanomax	0203	1
DAQ Chassis	National Instruments	cDAQ 9174	1
Analog Input Module	National Instruments	NI 9219	1
Analog Output Module	National Instruments	NI 9265	1
Thermocouple Input Module	National Instruments	Ni 9213	1

Upon initialization of the LabVIEW control and measurement system, the program collects data of the following forms: air temperature passing over the anemometer, anemometer velocity, temperature distribution at the outlet of the test section (this consisted of seven thermocouples placed in 12 mm vertical increments), temperature at the bubble inlet, and the ambient temperature. The maximum temperature in the test section was then determined from the collected data and used as input to the PID controller for the heaters.

The first step of the PID control is to calculate the error between the user set temperature, T_{set} , and the current maximum temperature in the test section, $T_{MaxTestSection}$, as shown in Eq. (14).

$$Error = T_{set} - T_{MaxTestSection} \quad (14)$$

The PID terms were then calculated as shown in Eq. (15) - Eq. (17),

$$PTerm = Kp * Error \quad (15)$$

$$ITerm = Ki * Error * dT + ITerm_{i-1} \quad (16)$$

$$DTerm = Kd * \frac{Error - Error_{i-1}}{dt} \quad (17)$$

where $PTerm$ is the proportional term, Kp is the proportional gain, $ITerm$ is the integral term, Ki is the integral gain, $ITerm_{i-1}$ is the integral term from the previous iteration of the controller, Kd is the derivative term, $Error_{i-1}$ is the error from the previous iteration of the controller, and dt is the time between controller iterations.

The output of the controller was then calculated by summing the P term, I term, and D term as shown in Eq. (18).

$$PID_{output} = PTerm + ITerm + DTerm \quad (18)$$

If the output of the PID control is greater than or less than the maximum or minimum milliamp output signal that the NI 9265 module is capable of producing, then the PID output will be restricted to the physical limit of the NI 9265 module before being sent to the solid state power control.

After generating the signal, the LabVIEW program creates an array containing all of the collected data and the PID output before plotting the wind tunnel temperature as a function of time and the test section temperature distribution as a function of the vertical position in the test section. The graphical user interface (GUI) for the program is shown in Fig. A4.

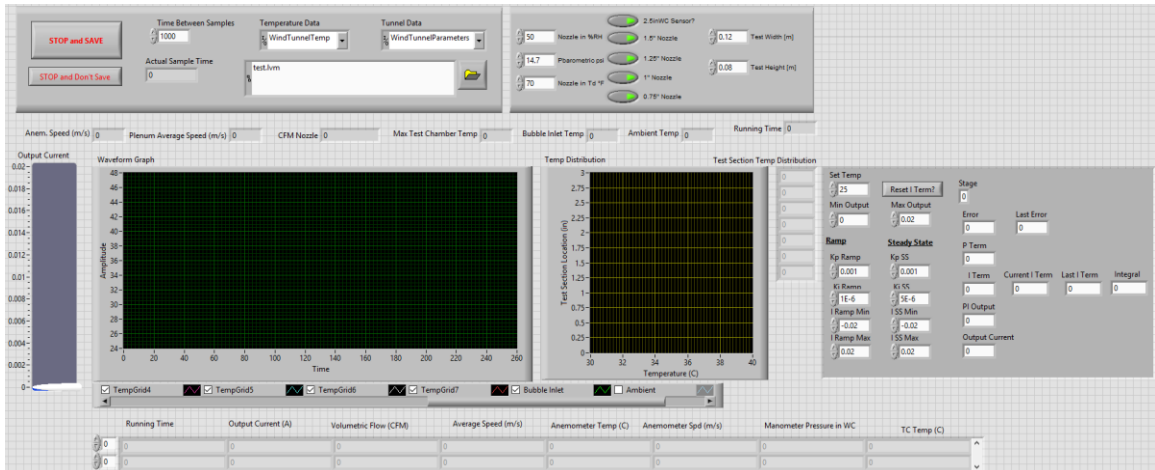


Fig. A4 Graphical user interface for the LabVIEW system

After plotting the collected data, the LabVIEW program checks to see if the user has stopped the program, and if “Stop and Save” button has been pressed, the controller will turn the heaters off before saving the data to a user specified file. The complete flow diagram for the control and measurement system is shown in Fig. A5.

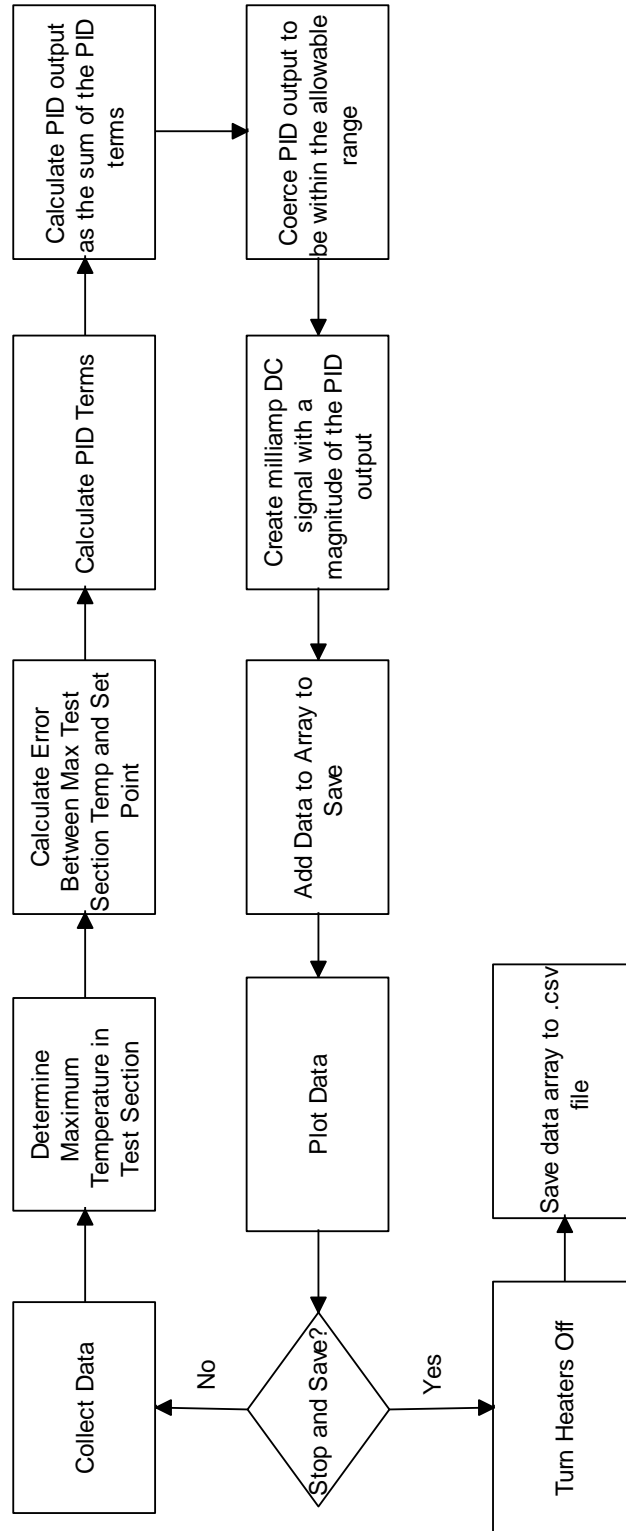


Fig. A5 Flow Diagram for LabVIEW control and measurement system

Appendix III: Flow Visualization System

The basis for the flow visualization system used for this study was developed by Tanquero [1], and consists of a helium filled soap bubble generator developed by Sage Action Inc., an LED light source, a high-speed camera, and a MATLAB image processing software program. Full details on the system may be found in section 3.3, “Flow Visualization System,” while a BOM of the components is given in Table A4.

Table A4: Flow Visualization BOM

Item	Manufacturer	Part Number	Qty
Light Source	See Tanquero	N/A	1
HFSB Generator	Sage Action, Inc	SAE Model 5 Helium Bubble Generator	1
Bubble Solution	Sage Action, Inc	SAI 1035	1
Helium Gas	Welder's Supply	N/A	1
Tripod	SunPak	7575	1
Camera	Sony	DSC-RX100M4	1
Memory Card	SanDisk	SDSDXWF-064G-ANCIN	1
MATLAB	Mathworks	N/A	1
Computer Vision System Toolbox	Mathworks	N/A	1

The MATLAB image processing software was initially developed from the Mathwork’s Motion-Based Multiple Object Tracking open source project by Tanquero [1]. However, to improve functionality, several changes were made to

Tanquero's program. Velocity calculations and plots were changed to utilize u-velocity components in the x-direction and v-velocity components in the y-direction, allowing for more clear velocity plotting and determination of the overall velocity magnitude and direction. Additionally, functionality was added to the program to enable calculation and plotting of the HFSB bubble count in both the x and y directions, as well as a summary document that details the maximum velocity, average velocity, total bubble count, and average bubble radius. These additional features enabled a better understanding of air temperature effects on bubble spatial distribution through the test section, the number of bubbles that survived at the elevated temperatures, and the impact of elevated temperatures on the v velocity component.

A complete flow chart for the MATLAB program is shown in Fig. A6. Upon beginning the program, the user is asked to select a video file. Once the file is selected, the program opens the first frame of the video on screen and prompts the user to select a grid size for the vector plot, select a reference distance, and apply a mask to remove noise from areas of non-interest in the video file.

Before further processing the video, the program creates empty arrays titled Vector Plot X, Vector Plot Y, Vector Plot U, and Vector Plot V. The columns in these arrays will specify a particular bubble, and the rows in the arrays will specify either the bubble x position, y position, calculated u velocity, or calculated v velocity for each detection of said bubble. The first image is then converted to an 8-bit greyscale image and a filter is applied to remove the foreground of the image.

Blobs are then identified as a clump of pixels differing from the foreground, from which the blob centroid and radius is calculated.

A Kalman filter is applied to determine the probability that the detected bubbles are new, or if they had been detected in a previous frame. If the blob is determined to be a new blob, a new column is added to the vector plot array and the blob centroid x position and y position, as well as the blob radius is recorded. If the blob had previously been detected, the blob's x position, y position, radius, u velocity, and v velocity are recorded as a new row in the blob's specified column in the vector plot arrays. The velocities are calculated by dividing the change in distance by the time between video frames, as shown in Eq. (19) and Eq. (20) respectively,

$$u_{xi} = \frac{x_i - x_{i-1}}{dt} \quad (19)$$

$$u_{yi} = \frac{y_i - y_{i-1}}{dt} \quad (20)$$

where u_{xi} and u_{yi} are the u and v velocity components respectively, x_i and y_i are the x and y coordinates of the bubble centroid for the given video frame, x_{i-1} and y_{i-1} are the x and y coordinates of the bubble centroid for the previous video frame, and dt is the time between video frames.

After calculating bubble velocities for the last frame of the video, the program begins post processing the data. To remove noise from the calculated velocity data caused by lighting reflections and bubbles passing in and out of the plane of interest, the program eliminates bubbles that have been detected in fewer than eight consecutive video frames per Tanquero's study [1]. The test section is

then divided into a grid with approximately 5 mm x 5 mm square areas to calculate the time based average velocity field. For each interrogation window in the grid, the MATLAB program sorts each detection of each bubble based on the recorded x and y centroid location. If the centroid location is within the physical bounds of said interrogation window, then that specific blob detection is included in the grid's average bubble velocity. In the cases where bubble velocities are low, it is possible that a bubble may be detected more than once in each grid. In these cases, each bubble detection is included in the interrogation window average velocity. Since each detection is a physical velocity that was measured in the given interrogation window, this method provides a more robust average velocity calculation that is less susceptible to noise or low bubble count. Interrogation windows in which zero detections were recorded are eliminated to enable clear plotting of the velocity field.

After calculating the velocity field, the program continues to determine bubble analytics. The total number of bubbles that were recorded for at least eight consecutive frames is recorded by counting the number of columns in the vector plot arrays. The bubble count in the y direction is determined by summing the bubbles with an average y centroid location within each row of the grid. Similarly, the bubble count in the x direction was determined by summing the number of bubble detections in each column of the grid. It should be clarified that the bubble count in the y direction is counting an actual number of bubbles, while the count in the x direction is counting the number of detections, which may count the same bubble multiple times in a column for low velocity flows.

Plots of the bubble count in the x and y direction were generated, as well as plots of the bubble velocity field and the test section centerline velocity profile. Lastly, the summary data file was created, and all arrays were saved as .csv files in a user specified folder.

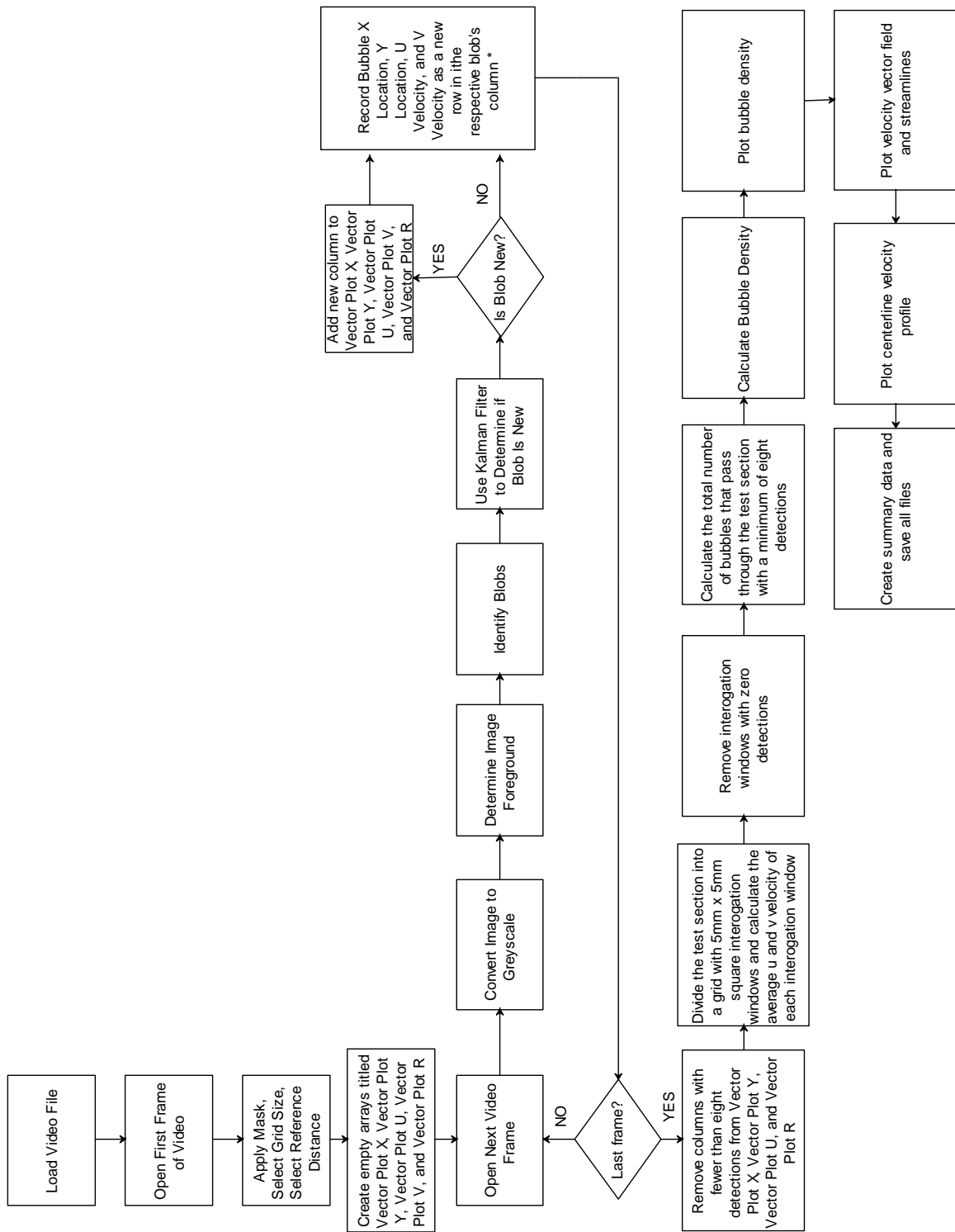


Fig. A6 MATLAB image processing program flow chart

Numerous arrays and data files are saved for each processed video. A summary of the saved data files may be found in Table A5.

Table A5: Data Files Exported by MATLAB program.

File Name	Summary
BubbleDensityX.csv	A two-column array in which the first column provides the x position of the centerline for each column of the grid and the second column provides the count for the number of detections in said column of the grid.
BubbleDensityX.png	A plot of the data in BubbleDensityX.csv, in which the number of detections is plotted on the y axis and the x position is plotted on the x axis.
BubbleDensityY.csv	A two-column array in which the first column provides the y position of the centerline for each row of the grid and the second column provides the count for the number of bubbles in said row of the grid.
BubbleDensityY.png	A plot of the data in BubbleDensityY.csv, in which the number of bubbles is plotted on the x axis and the y position is plotted on the y axis.
CenterlineVelocityProfile.png	A plot of the velocity profile of the middle most column of the grid, in which the velocity is plotted on the x axis and the y position is plotted on the y axis.
CountourPlotMatrixU.csv	An array in which the u velocity component is recorded for each interrogation window of the grid.
CountourPlotMatrixUsmooth.csv	An array in which the u velocity component is recorded for each interrogation window of the grid after a smoothing algorithm has been applied to reduce discontinuities.
CountourPlotMatrixV.csv	An array in which the v velocity component is recorded for each interrogation window of the grid.
CountourPlotMatrixVsmooth.csv	An array in which the V velocity component is recorded for each interrogation window of the grid after a smoothing algorithm has been applied to reduce discontinuities.
CountourPlotMatrixX.csv	An array in which the x position is recorded for each interrogation window of the grid.
CountourPlotMatrixY.csv	An array in which the y position is recorded for each interrogation window of the grid.
Flowlines Image.png	A plot of the flowlines of the fluid flow in the region of interest.

FullVectorPlot.csv	An array containing information for each detection of each bubble. Each row represents a new detection while the columns represent the x position, y position, u velocity, v velocity, the video frame number, and the blob radius in that order. This array has not eliminated bubbles that have been detected in fewer eight consecutive frames.
PlotMatrix.csv	An array combining the four different contour plot arrays. The columns contain the x position to be plotted for the vector field, the y position to be plotted for the vector field, the u velocity component, the v velocity component, the velocity magnitude, and the ratio of the v velocity over the u velocity component respectively.
Summary.csv	A single column array in which the rows represent the total bubble count, the maximum recorded u velocity, the average velocity of the centerline profile, the average v velocity component, and the v velocity component standard deviation respectively.
VectorPlot.png	A plot of the vector field in the area of interest.
VectorPlotR.csv	An array indicating the blob radius for each detection of each bubble. Each column represents a new bubble and each row represents a detection of said bubble. This array has not eliminated bubbles that have been detected in fewer than eight consecutive frames.
VectorPlotT.csv	An array indicating the video frame number for each detection of each bubble. Each column represents a new bubble and each row represents a detection of said bubble. This array has not eliminated bubbles that have been detected in fewer than eight consecutive frames.
VectorPlotTestU.csv	An array indicating the u velocity component for each detection of each bubble. Each column represents a new bubble and each row represents a detection of said bubble. Bubbles that have been detected in fewer than eight consecutive frames are removed from this array.

VectorPlotTestV.csv	An array indicating the v velocity component for each detection of each bubble. Each column represents a new bubble and each row represents a detection of said bubble. Bubbles that have been detected in fewer than eight consecutive frames are removed from this array.
VectorPlotTestX.csv	An array indicating the x position of the blob centroid for each detection of each bubble. Each column represents a new bubble and each row represents a detection of said bubble. Bubbles that have been detected in fewer than eight consecutive frames are removed from this array.
VectorPlotTestY.csv	An array indicating the y position of the blob centroid for each detection of each bubble. Each column represents a new bubble and each row represents a detection of said bubble. Bubbles that have been detected in fewer than eight consecutive frames are removed from this array.
VectorPlotU.csv	An array indicating the u velocity component for each detection of each bubble. Each column represents a new bubble and each row represents a detection of said bubble. This array has not eliminated bubbles that have been detected in fewer than eight consecutive frames.
VectorPlotV.csv	An array indicating the v velocity component for each detection of each bubble. Each column represents a new bubble and each row represents a detection of said bubble. This array has not eliminated bubbles that have been detected in fewer than eight consecutive frames.
VectorPlotX.csv	An array indicating the x position of the blob centroid for each detection of each bubble. Each column represents a new bubble and each row represents a detection of said bubble. This array has not eliminated bubbles that have been detected in fewer than eight consecutive frames.
VectorPlotX.png	A plot of the u velocity vector field in the area of interest.
VectorPlotY.csv	An array indicating the y position of the blob centroid for each detection of each bubble. Each column represents a new bubble and each row represents a detection of said bubble. This array has not eliminated bubbles that have been detected in fewer than eight consecutive frames.
VectorPlotY.png	A plot of the v velocity vector field in the area of interest.

Appendix IV: Results

The main conclusions and results from the study are detailed in Section 4, “Results” found above. Additional centerline velocity profile plots are shown below for each flow velocity tested, as well as bubble count plots in the y direction in Fig. A7 through Fig. A16.

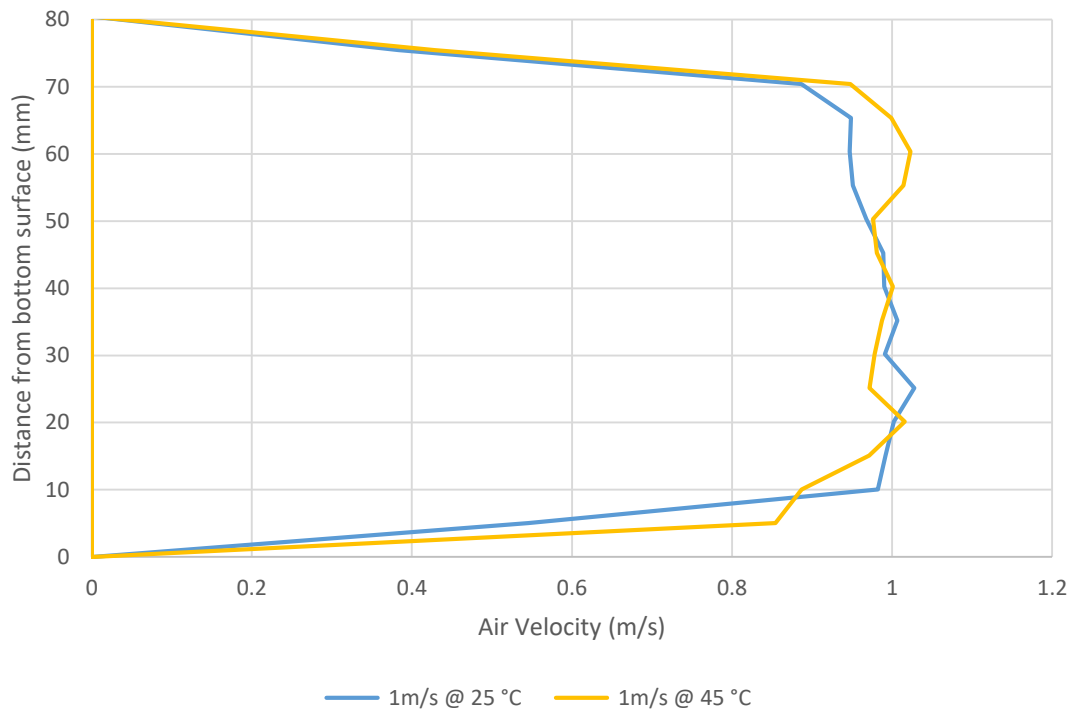


Fig. A7 Centerline velocity profile for the 1 m/s flow scenario

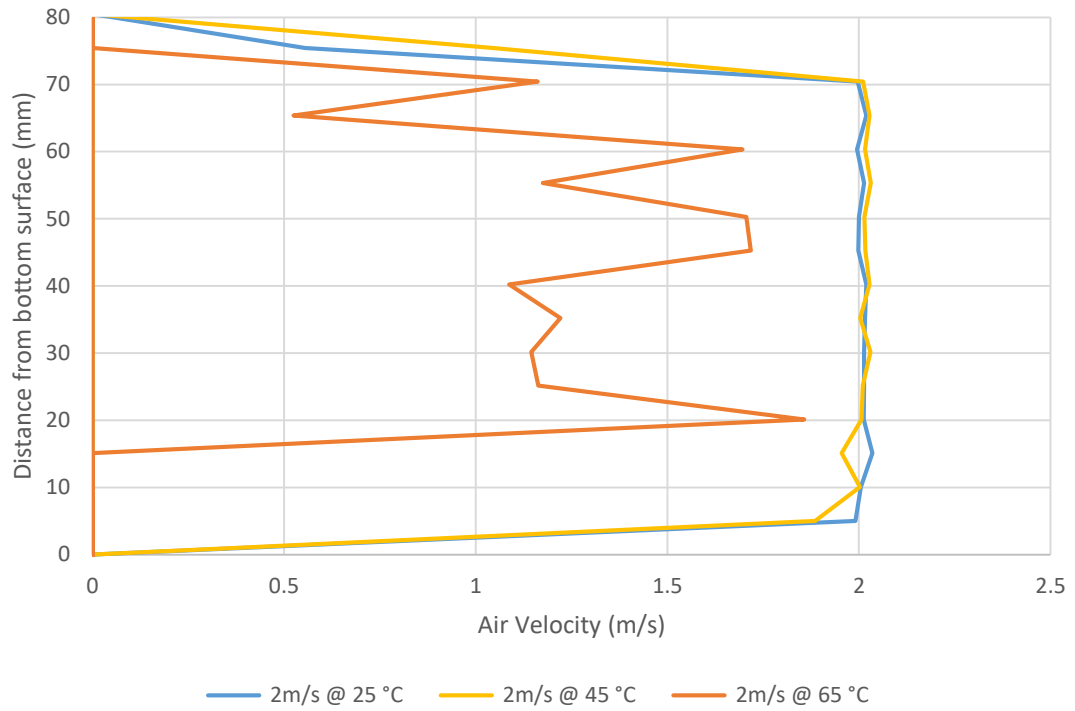


Fig. A8 Centerline velocity profile for the 2 m/s flow scenario

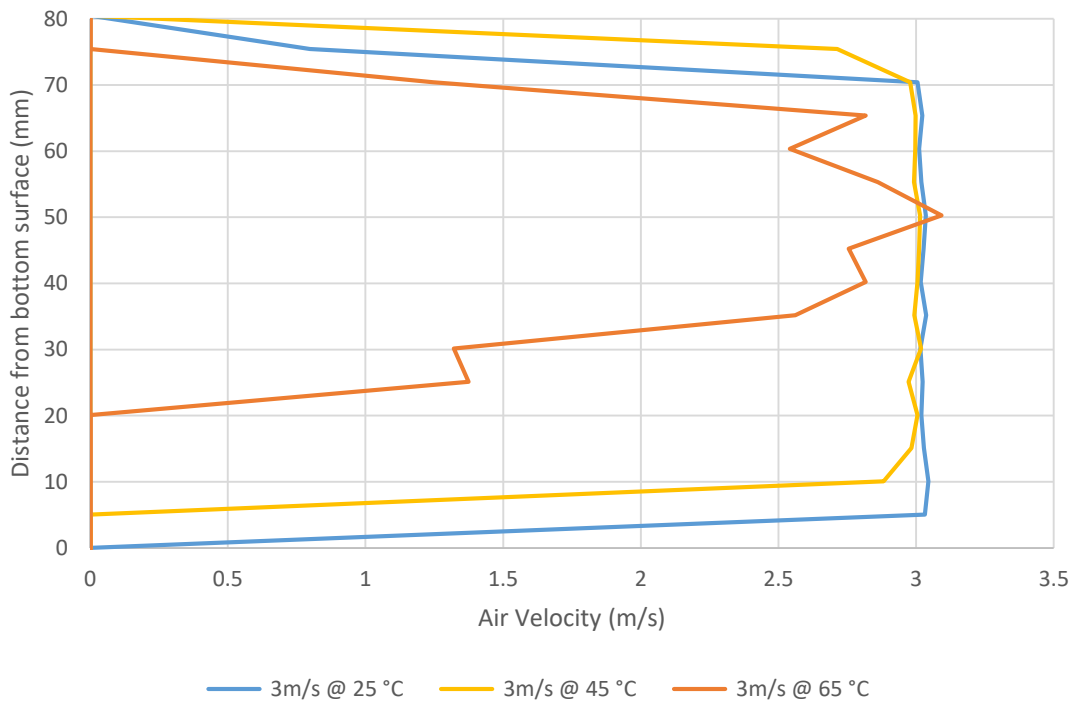


Fig. A9 Centerline velocity profile for the 3 m/s flow scenario

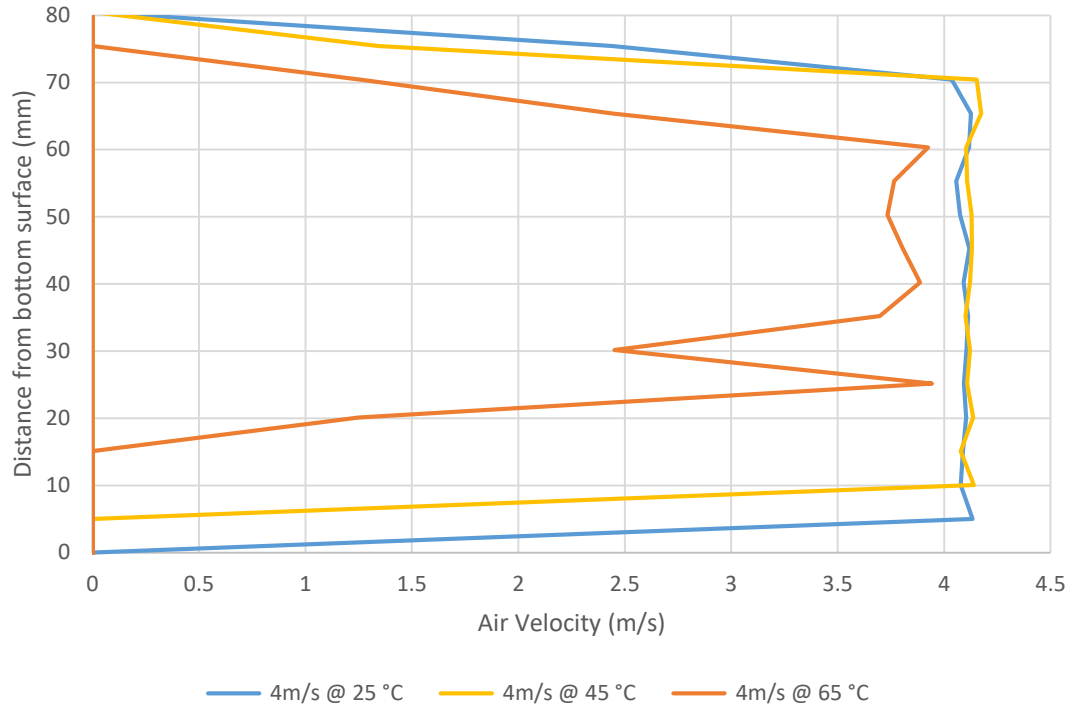


Fig. A10 Centerline velocity profile for the 4 m/s flow scenario

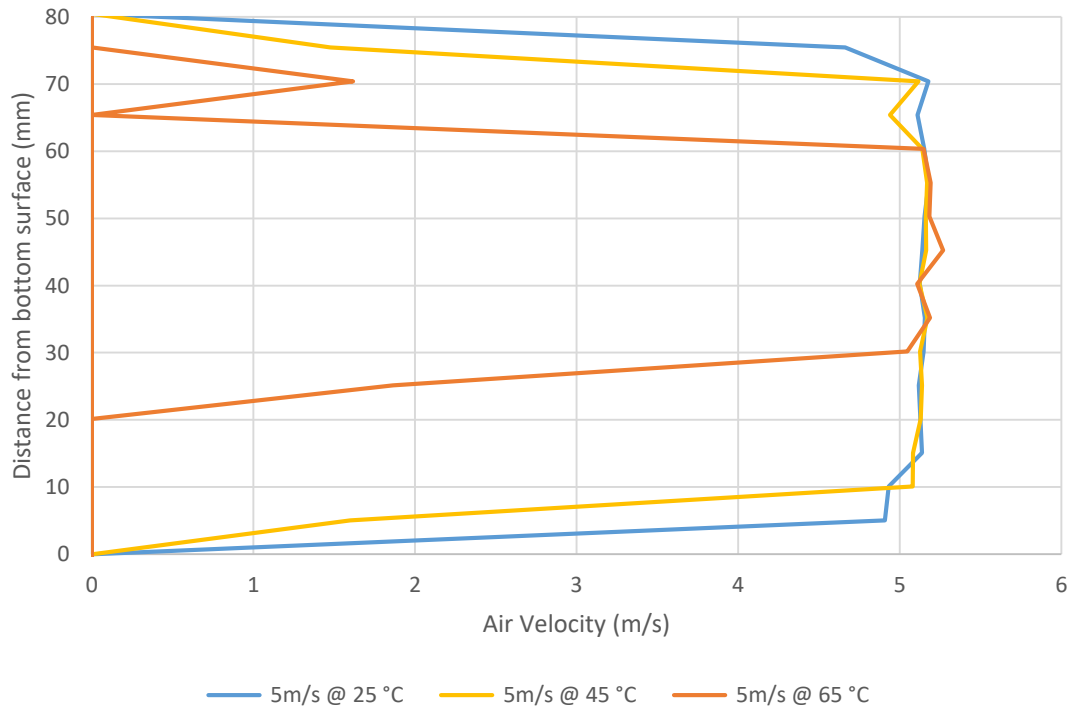


Fig. A11 Centerline velocity profile for the 5 m/s flow scenario

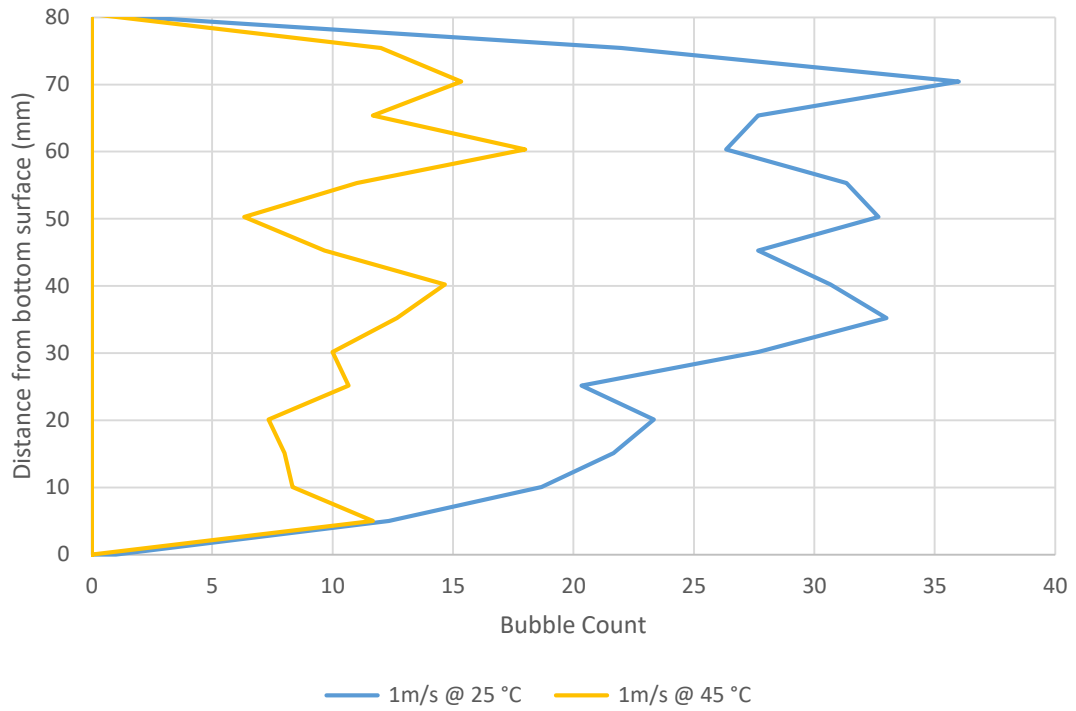


Fig. A12 Bubble count in the y direction for the 1 m/s flow scenario

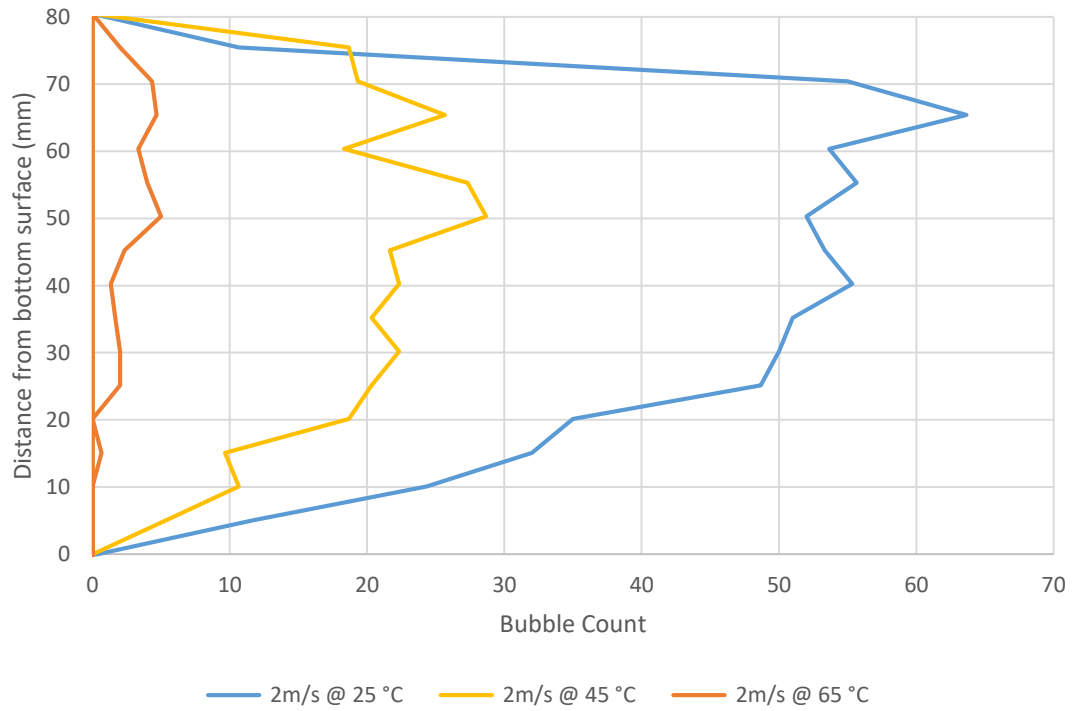


Fig. A13 Bubble count in the y direction for the 2 m/s flow scenario

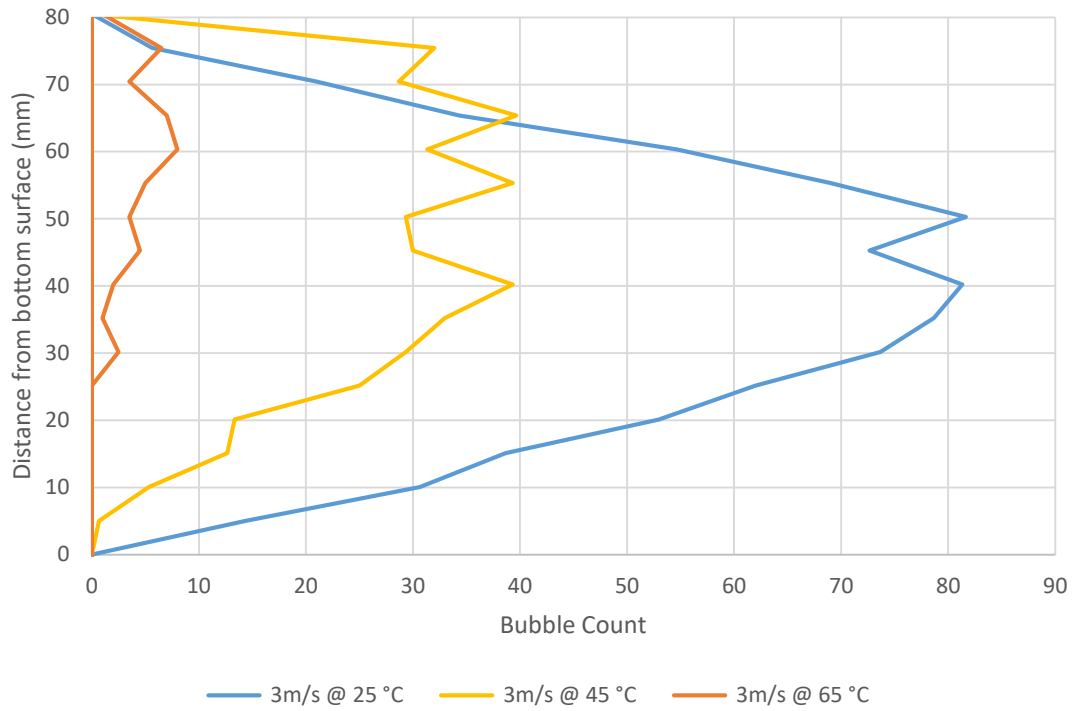


Fig. A14 Bubble count in the y direction for the 3 m/s flow scenario

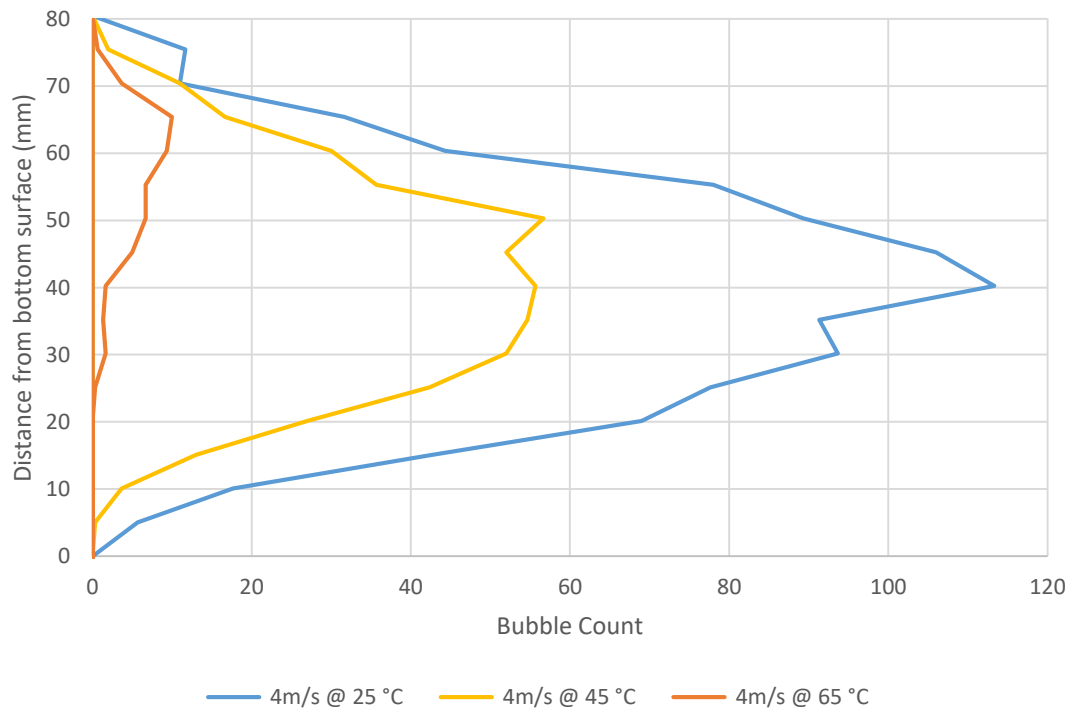


Fig. A15 Bubble count in the y direction for the 4 m/s flow scenario

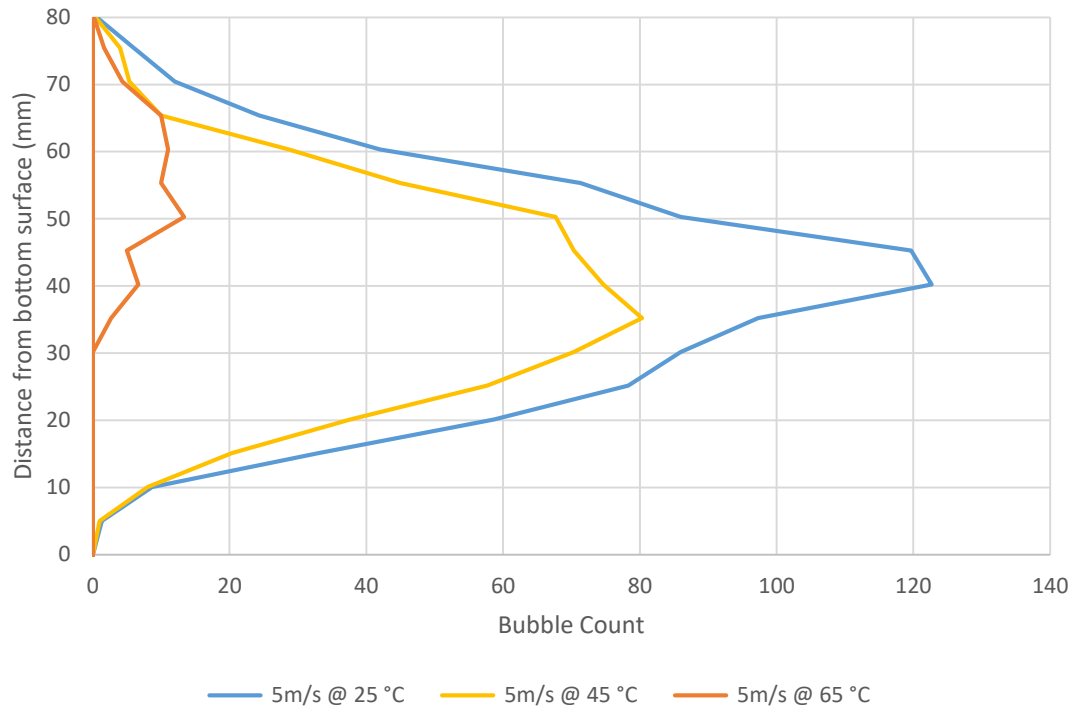


Fig. A16 Bubble count in the y direction for the 5 m/s flow scenario

Appendix V: Discussion of Heater Induced Buoyancy

As previously mentioned in the results, at increased temperatures, the centerline velocity profiles and the bubble densities experience a shift in the positive y direction, where y is defined positive upward. This shift is due to natural convection that occurs at the heaters as cool air slowly moves past the hot fins. To quantify this effect, the ratio of the Grashoff number to the square of Reynolds number is calculated to quantify the relative contributions of forced versus free convection. If $\frac{Gr}{Re^2} \gg 1$, the natural convection dominates the flow, while if $\frac{Gr}{Re^2} \ll 1$, then forced convection dominates the flow. In cases where $\frac{Gr}{Re^2} \approx 1$, both natural and forced convection are significant.

To calculate the ratio of the Grashoff number to the square of Reynolds number, first the fin temperature of the heater must be calculated. Assuming negligible radiation to the surrounding environment, constant material properties, and negligible heat transfer from the edges of the fins, an energy balance may be written per unit area of fin as shown below in Eq. (21).

$$q''_{electrical} = q''_{MixedConvection} \quad (21)$$

The mixed convection term may be expanded through Newton's Law of Cooling, given in Eq. (22), where h_{eff} is the effective convective heat transfer coefficient for mixed convective flows, T_s is the fin surface temperature, and T_∞ is the free stream temperature.

$$q''_{MixedConvection} = h_{eff}(T_s - T_{\infty}) \quad (22)$$

The effective heat transfer coefficient was found using a Nusselt correlation for mixed convection heat transfer, shown below in Eq. (23) and Eq. (24),

$$h_{eff} = \frac{Nu_{eff}k}{D_h} \quad (23)$$

$$Nu_{eff} = [Nu_F^n + Nu_N^n]^{\frac{1}{n}} \quad (24)$$

where Nu_{eff} is the effective Nusselt number, k is the thermal conductivity of air, D_h is the hydraulic diameter for flow through fins as shown in Eq. (25), in which S is the gap between fins, n is a constant dependent on the flow geometry and was assumed to be 4 for this application [17], Nu_F is the Nusselt number for the forced convection, and Nu_N is the Nusselt number for the natural or free convection.

$$D_h = \frac{S}{2} \quad (25)$$

The Nusselt number for forced convection between two parallel plates is given in Eq. (26), in which the Reynolds number is defined as shown in Eq. (27) and w represents the length of the fin in the direction of the forced air flow.

$$Nu_F = 7.54 + \frac{0.03 \left(\frac{D_h}{w}\right) RePr}{1 + 0.016 \left[\left(\frac{D_h}{w}\right) RePr\right]^{2/3}} \quad (26)$$

$$Re = \frac{u_{\infty} D_h}{\nu} \quad (27)$$

Similarly, the Bar-Cohen Nusselt correlation was used to determine the free convection heat transfer coefficient as shown in Eq. (28).

$$Nu_N = \left[\frac{C_1}{\left(\frac{Ra_s S}{L}\right)^2} + \frac{C_2}{\left(\frac{Ra_s S}{L}\right)^{\frac{1}{2}}} \right]^{-1/2} \quad (28)$$

where the constants C_1 and C_2 are given as 576 and 2.87 respectively for symmetric isothermal plates [17], L is the vertical height of the fin, and Ra_s is defined in Eq. (29) where g represents the gravitational constant, β is volumetric thermal expansion coefficient, α is the thermal diffusivity of the fluid, and ν is the kinematic viscosity of the fluid.

$$Ra_s = \frac{g\beta(T_s - T_\infty)S^3}{\alpha\nu} \quad (29)$$

An iterative approach was implemented in which the fin surface temperature, T_s , was varied until Eq. (21) was valid within at least three significant figures, providing a fin temperature, T_s , of 330 °C for the lowest tested flow velocity. It should be noted that due to the larger cross-sectional area of the heating chamber compared to the test section, the minimum test flow velocity of 1 m/s through the test section resulted in a flow velocity of 0.175 m/s through the heating chamber.

The calculated fin temperature was compared with the manufacturer provided plot of fin temperature verses watt density for several different flow velocities, shown in Fig. A17. At the operating velocity of 0.175 m/s and a power density of 3.1 W/cm², as shown by the blue dot on Fig. A17, the manufacturer suggests the fins will reach a temperature of approximately 440 °C (713 K), which

is within 15 percent of the calculated fin temperature of 330 °C (600 K) shown by the yellow triangle, validating the theoretical model.

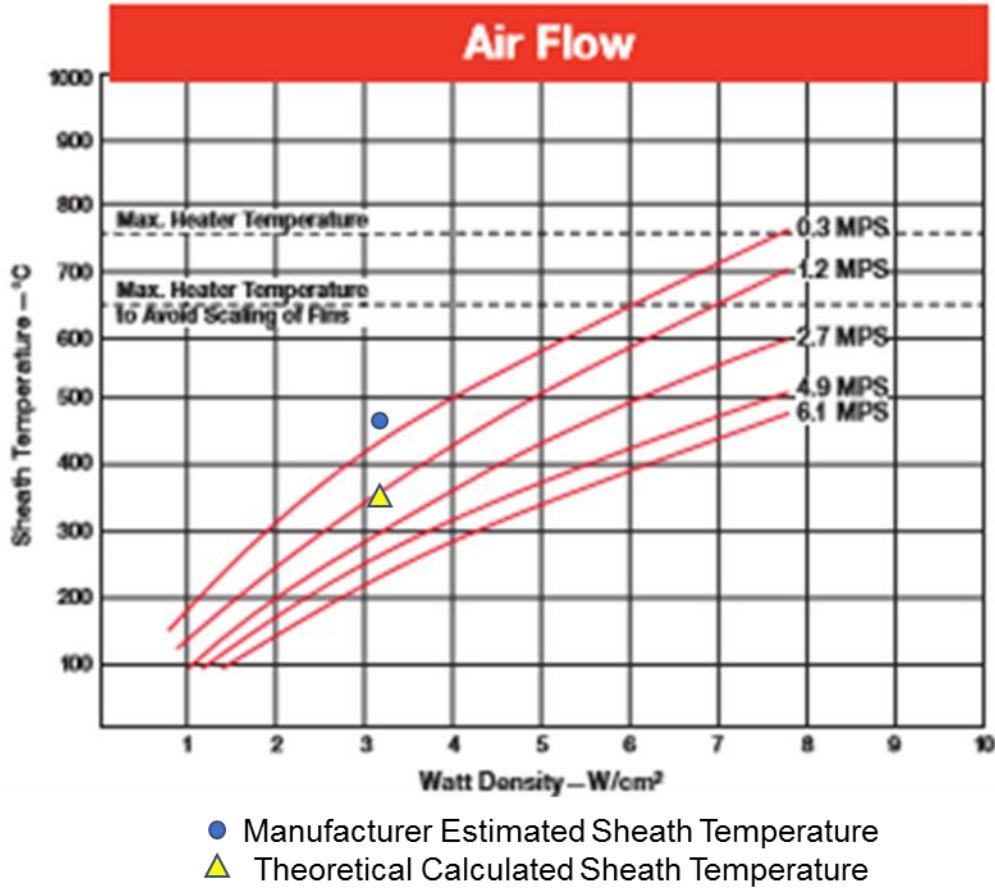


Fig. A17 Heater fin temperature for various power densities [18]

The ratio of the Grashoff number to the square of Reynolds number was then calculated as shown in Eq. (30).

$$\frac{Gr}{Re^2} = \frac{g\beta(T_s - T_\infty)D_h}{u_\infty^2} \quad (30)$$

At the lowest tested flow velocities, the ratio, $\frac{Gr}{Re^2}$, was approximately 0.6, indicating that both natural and forced convection are significant in this application, and buoyant effects will cause flow stratification over the heaters.

The effect of natural convection on flow stratification is further confirmed by analyzing the plot of the temperature distribution in the test section, shown in Fig. A18. Elevated temperatures are found at the top of the test section, indicating the flow stratification that occurred through the length of the test section as a result of natural convection at the heaters.

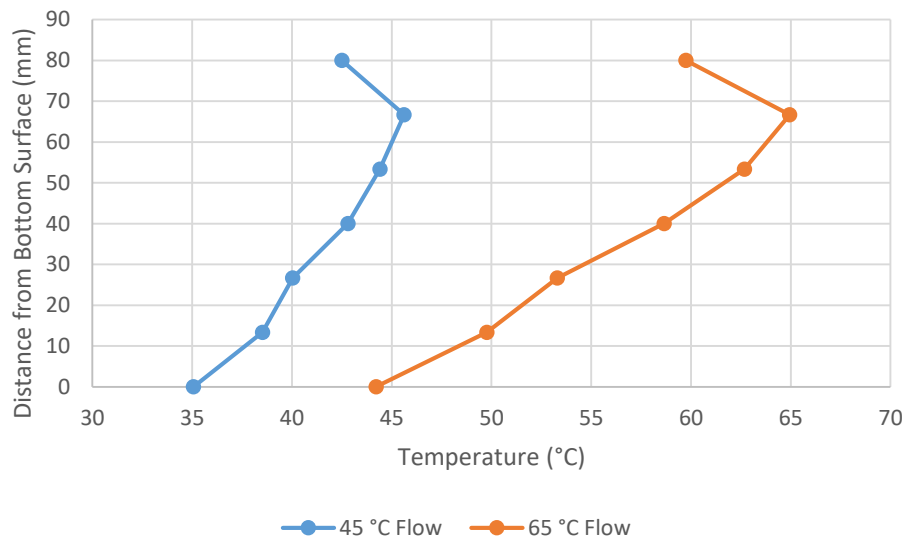


Fig. A18 Temperature distribution in the test section for 3 m/s flow

Appendix VI: Investigation of Boundary Layer Discernment

An additional potential use of HFSB PTV systems is the discernment of boundary layers in the flow field of interest. To understand the capability of the system used in this study to discern the boundary layer, the boundary layer thickness was calculated for turbulent flow over an isothermal plate for each of the flow velocities using Eq. (31), where δ is the boundary layer thickness, x is the leading edge of the flow, which for this study was taken to be the midplane of the constriction [9], and Re_x is the Reynolds number calculated using the distance parameter x as the characteristic length.

$$\delta = 0.37xRe_x^{-1/5} \quad (31)$$

The velocity profile in the boundary layer was then determined using the one-seventh power law, given in Eq. (32), where u is the local velocity, u_∞ is the free stream velocity, and y is the distance from the wall.

$$u = u_\infty \left(\frac{y}{\delta}\right)^{1/7} \quad (32)$$

The theoretical boundary layer velocity profile calculated in Eq. (32) was plotted in comparison to the experimental velocity profiles for the 25 °C and 45 °C flow cases for each velocity tested, as shown in Fig. A19 through Fig. A23.

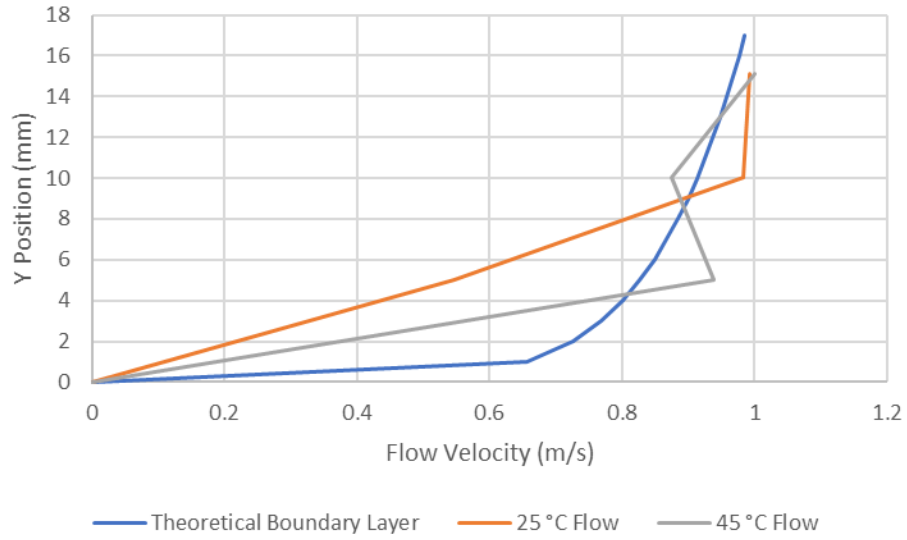


Fig. A19 Boundary layer velocity profile for the 1 m/s flow scenario

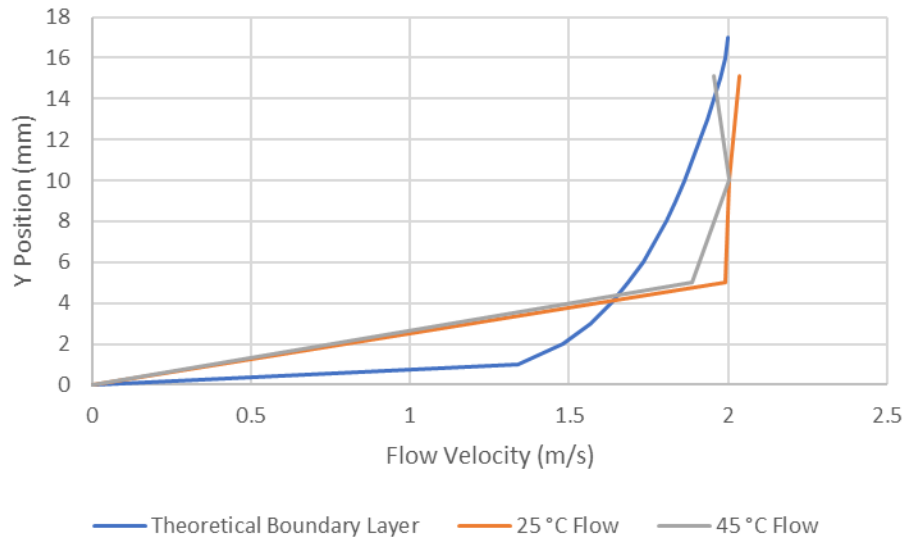


Fig. A20 Boundary layer velocity profile for the 2 m/s flow scenario

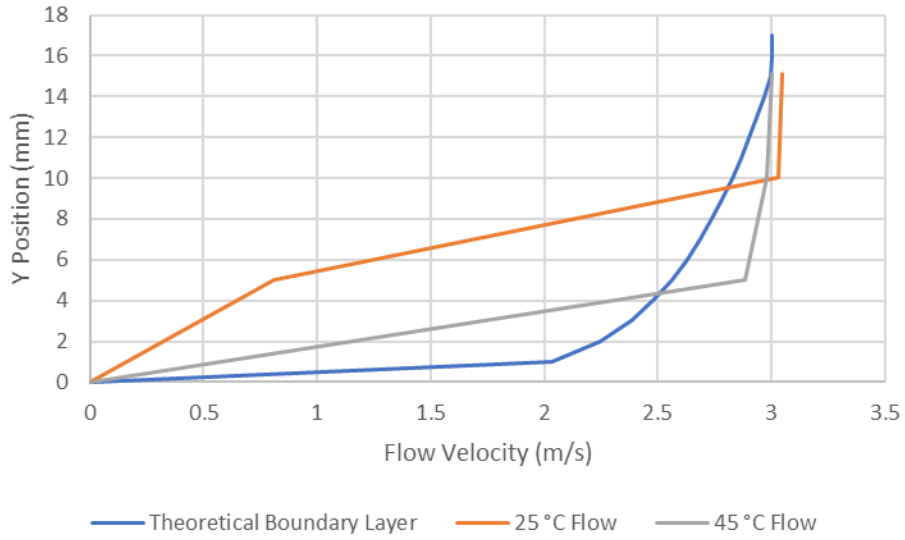


Fig. A21 Boundary layer velocity profile for the 3 m/s flow scenario

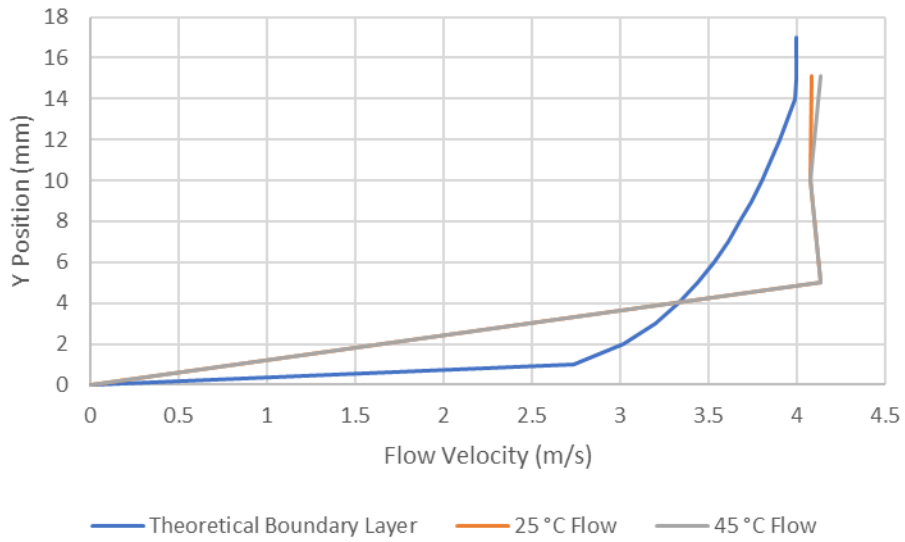


Fig. A22 Boundary layer velocity profile for the 4 m/s flow scenario

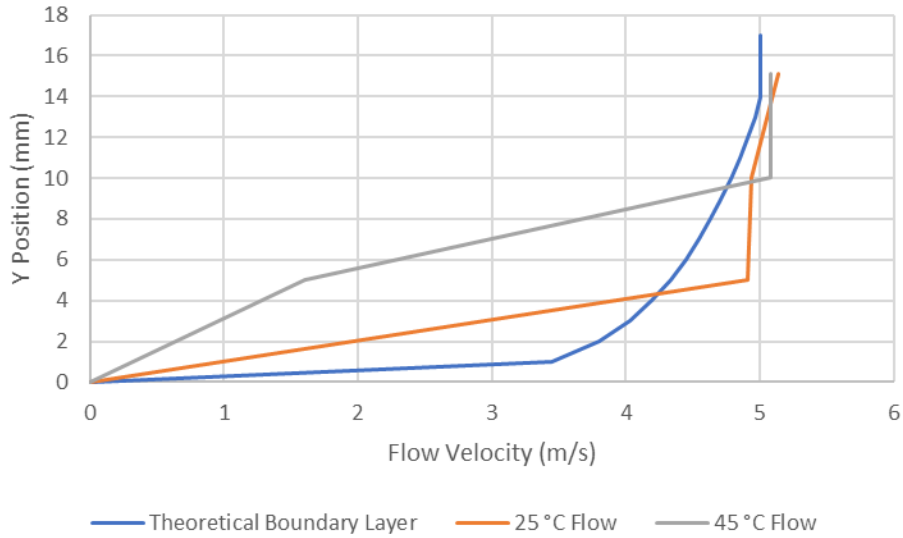


Fig. A23 Boundary layer velocity profile for the 5 m/s flow scenario

As seen in Fig. A19 through Fig. A23, the PTV measurement system used in this study yields large errors in the measured velocity in the boundary layer of the flow, in some cases in excess of 100 percent. This is due to the low bubble density near the walls of the test section, in which there were often fewer than ten bubbles. At a distance equal to or greater than the boundary layer thickness, however, the bubble count is sufficient to provide reliable velocity measurements across the entire free stream region. Further analysis of Fig. A12 - Fig. A16 show that for most test cases, fewer than twenty bubbles were detected in the interrogation windows in the boundary layer. Therefore, it is suggested that for valid velocity measurements, a minimum of twenty bubbles must pass through each interrogation window. As such, the system highlighted in this study should only be used for free stream velocity measurements.

Appendix VII: Effects of Temperature on Bubble Life

An additional conclusion from the study indicates that at elevated temperatures, HF SBs have a shorter life. Several hypotheses exist to explain why bubbles at elevated temperatures pop faster than bubbles at ambient temperatures. One such hypothesis suggests that at elevated temperatures, the bubble film solution will evaporate faster than at lower temperatures. As such, the bubble wall thins faster, increasing the stress caused on the bubble wall by the internal pressure of the helium gas, ultimately causing the bubble to pop.

An alternative hypothesis states that at elevated temperatures, assuming negligible heat transfer to the helium gas filling the bubble, the exterior air pressure will increase as temperature increases, creating a compressive stress on the bubble surface that ultimately causes the bubble to implode. Such a physical phenomenon may be visible as a decrease in the bubble diameter.

Therefore, in an attempt to understand which hypothesis accurately describes the physics, the average bubble diameter was plotted for each temperature tested as a function of flow velocity, shown in Fig. A24. With the exception of the 65 °C test case in which too few bubbles were recorded for valid analysis, the bubble diameter appeared independent of flow temperature, but increasing with increasing flow velocity.

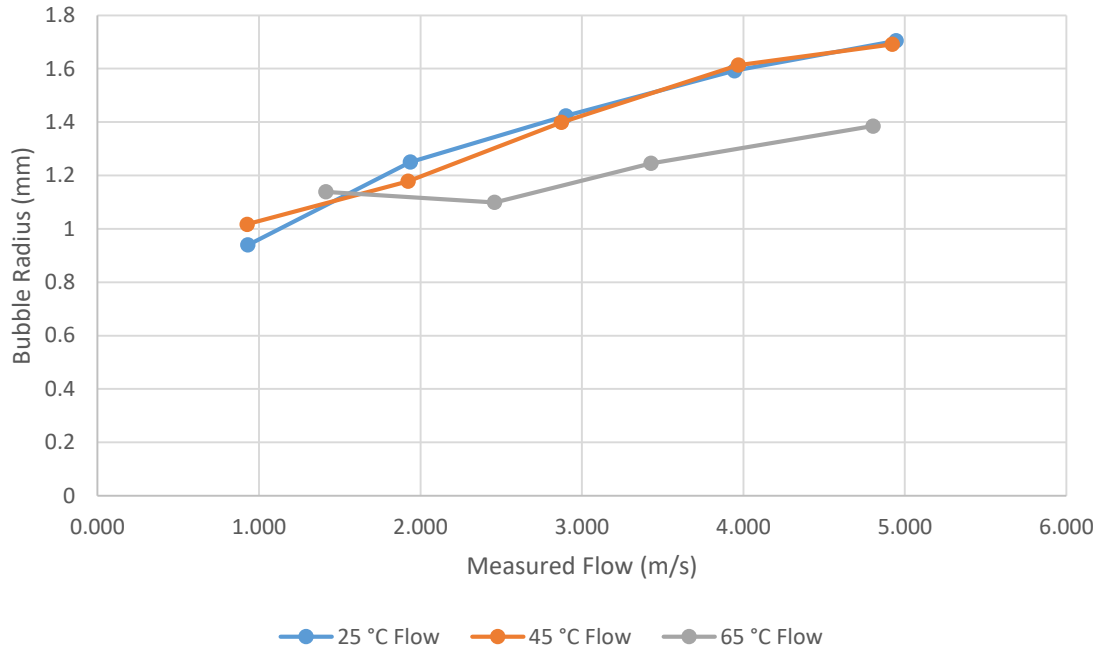


Fig. A24 Bubble radius as a function of temperature and flow velocity.

However, upon closer inspection of the MATLAB program, the increase in bubble radius as a function of flow speed is invalid. In calculating the blob radius, the MATLAB program assumes that each blob is a sphere. In high flow velocities though, the video frame rate is too slow to capture the bubbles as spheres, and instead the bubbles are recorded as ellipses. This phenomenon is shown below in Fig. A25 and Fig. A26. The apparent ellipse shape of bubbles at high velocities causes the program to overestimate the blob radius.

Since the bubble radii are the same throughout the 25 °C and 45 °C test cases, it does not appear that the increase in air pressure surrounding the bubble causes any significant changes in bubbles size. Instead, it appears that the increased evaporation rate of the bubble soap solution may be the leading factor

in the decreased bubble survival rate at high temperatures, although further studies are needed to confirm this result.

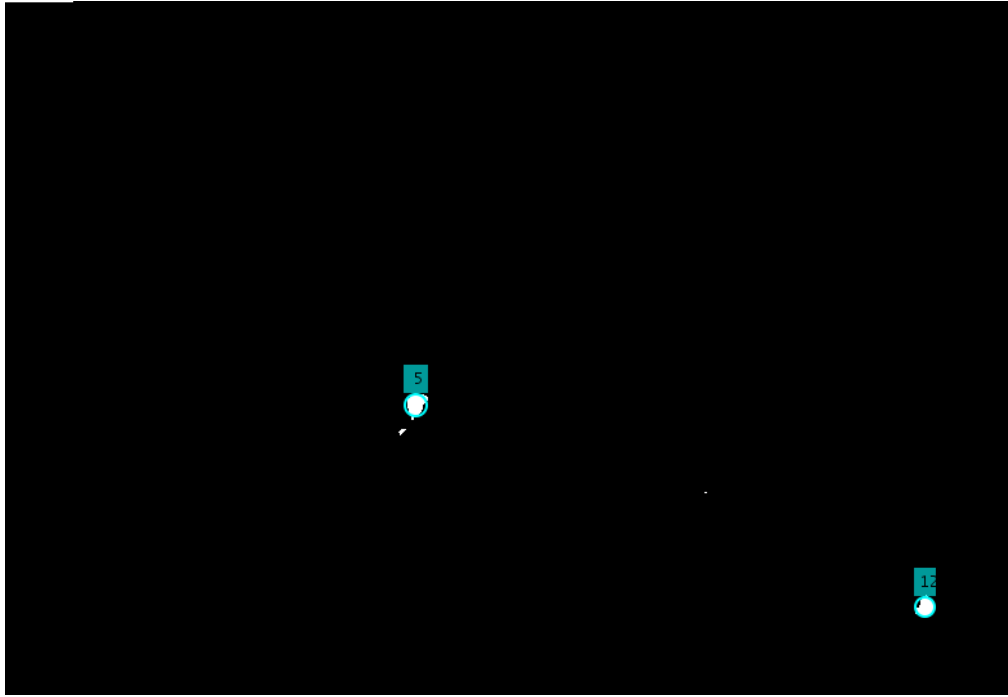


Fig. A25 MATLAB bubble detection for 1 m/s 25 °C flow.

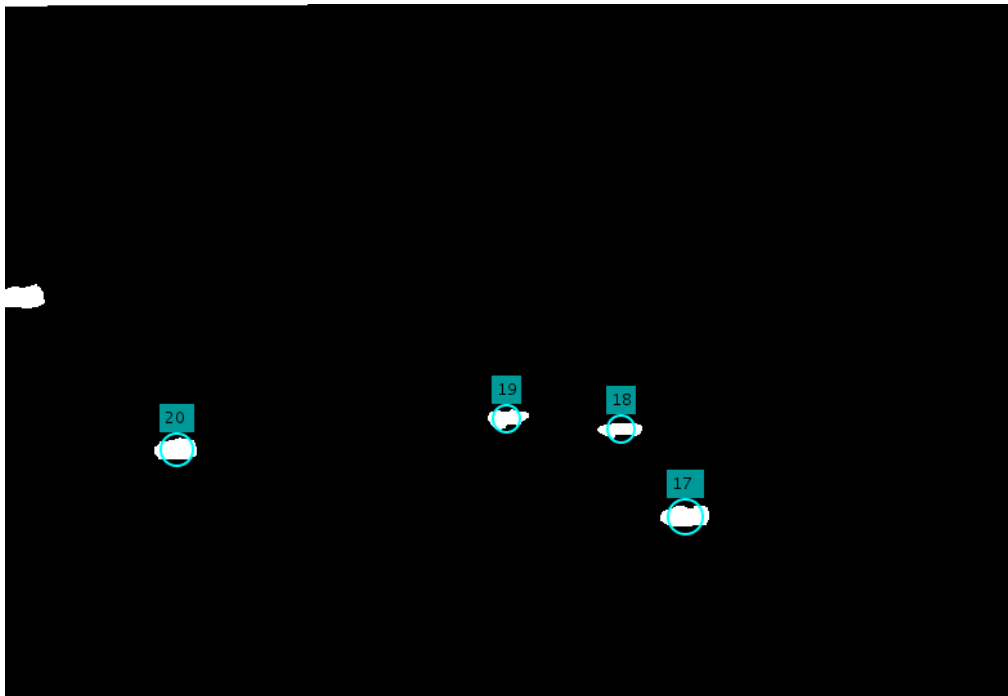


Fig. A26 MATLAB bubble detection for 5 m/s 25 °C flow.

CURRICULUM VITA

NAME: Michael Blum

CONTACT INFORMATION: 1144 Audubon Pkwy, Louisville, KY 40213
Work: 502-452-4028
Cell: 502-396-4029
Michael.blum13@gmail.com

DOB: May 13, 1993

EDUCATION & TRAINING

M.S. Mechanical Engineering (exp. 08/2018)
University of Louisville
(GPA: 4.0/4.0)
2016-2018

B.S. Mechanical Engineering
University of Kentucky
(GPA: 4.0/4.0)
2011-2015

B.S. Mathematics
University of Kentucky
(GPA: 4.0/4.0)
2011-2015

WORK EXPERIENCE:

GE Appliances, Louisville, KY January 2016-Present
Edison Engineering Development Program

4th Rotation: Range, Advanced Systems July 2017-Present

- Developed control systems and algorithms for cooktop closed loop cooking on radiant, gas, and induction platforms
- Designed and developed a combined RTD and monopole antenna for a SAW wireless meat probe
- Submitted 5 patent applications
- Studied temperature effects on helium filled soap bubble particle tracking velocimetry

3rd Rotation: Laundry, Advanced Systems January 2017-July 2017

- Responsible for the development of the 2019 top load washer drive system utilizing a PMSM
- Responsible for sound testing, power testing, heat rise testing, and motor control development
- Developed several LabVIEW programs and test stands for data acquisition and analysis

2nd Rotation: Field Returns Lab July 2016-January 2017

- Led investigation of top load washer out of balance and developed an algorithm to continuously monitor system mass moment of inertia
- Responsible for weekly product teardowns and root cause analysis
- Participated in scene inspections for appliance field failures
- Attended Fire Investigation Training
- Submitted one patent application

1st Rotation: Range, Product Cost Takeout January 2016-July 2016

- Responsible for several product cost take out projects worth a total annual savings of over \$1 million
- Initiated a design for six sigma (DFSS) study of the gas safety valve
- Developed a test fixture to understand the effects of radiation and convection on cabinet temperature surrounding gas ranges

GE Appliances, Louisville, KY
Technology Coop

August 2012-August 2015

3rd Rotation: Gas Range, Cooking Performance

May 2015-August 2015

- Completed a design of experiments (DOE) to study the effects of cooking temperature, power cycling, and convection fan on time on cooking performance
- Build a prototype gas range with a front cavity vent to study the effects of combustion product gas flow on cooking performance
- Studied the effects of glow bar key noise parameters to optimize burner cycling for improved cooking performance

2nd Rotation: Advanced Development

May 2014-August 2014

- Responsible for safety agency range anti-tip requirement compliance
- Developed a statics model of the EZ Slide oven door to analyze tipping capabilities and develop design solutions
- Responsible for the torsion spring design and manufacturing for the door of EZ Slide Oven Drawer

1st Rotation: Laundry, Dryer Airflow

August 2013-Dec. 2013

- Completed a root cause investigation of particle accumulation on fan blades
- Developed installation guides for long vent dryer installations

University of Kentucky, Lexington, KY
Engineering Tutor

August 2014-Dec. 2015

- Tutored engineering students in the areas of calculus, thermodynamics, heat transfer, systems, controls, statics, dynamics, and vibrations.

Toyota, Georgetown, KY

May 2012-August 2013

Quality Engineering Coop

- Responsible for maintaining supplier and part quality for vehicle interior and door parts
- Responsible for implementing short term counter measures, developing a root cause, and implementing long term counter measures
- Utilized the five why process, pareto charts, and fishbone diagrams

TECHNICAL SKILLS:

- Data acquisition and test bed development
- Control system development
- Sensor Development
- Particle tracking velocimetry (PTV) measurements
- Rapid prototyping
- Root cause analysis
- 10 Step Design for Six Sigma Process

COMPUTER SKILL & LANGUAGES:

Proficient: LabVIEW, Arduino, MATLAB, Creo/ProE, Solidworks, Minitab, MS Excel, MS Word

Familiar: Git, C++, Visual Basic,